

The Dynamics of Ascent-Forced Orographic Convection in the Tropics: Results from Dominica*

JUSTIN R. MINDER, RONALD B. SMITH, AND ALISON D. NUGENT

Department of Geology and Geophysics, Yale University, New Haven, Connecticut

(Manuscript received 7 January 2013, in final form 12 July 2013)

ABSTRACT

The mountainous Caribbean island of Dominica was chosen as a natural laboratory for studying orographic convection in the tropics. Here, the authors focus on a prototypical case study, taken from the Dominica Experiment (DOMEX) field campaign in the spring of 2011. Airborne measurements and high-resolution numerical experiments are used to examine the mesoscale dynamics of moist airflow over Dominica and its relationship to convection, turbulence, and rainfall.

Upwind of the island, there is minimal lateral deflection or lifting of the flow, largely because of latent heat release in the overisland convection. Over the terrain, forced ascent leads to rapid development of moist convection, buoyancy-generated turbulence, and rainfall. Although this convection produces sporadic bursts of heavy rainfall, it does not appear to enhance the time-mean rainfall. Over the lee slopes, a dry plunging flow produces anisotropic shear-generated turbulence and strong low-level winds while quickly dissipating convection and rainfall. In the wake, low-level air is decelerated, both by turbulence in the plunging flow and by frictional drag over the island. Low-level wake air is also dried and warmed, primarily by turbulent vertical mixing and regional descent, both associated with the downslope flow. Rainfall and latent heating play only a secondary role in warming and drying the wake.

1. Introduction and background

Throughout the tropics and subtropics, topography has profound influences on the distribution of rainfall. These influences are particularly striking as characterized from space by the Tropical Rainfall Measurement Mission (TRMM)'s precipitation radar (PR). High-resolution climatologies from the TRMM PR show tight relationships between topographic features and both the intensity and diurnal phasing of rainfall down to scales of a few kilometers (Nesbitt and Anders 2009; Biasutti et al. 2012; Houze 2012). Despite these strong orographic controls on tropical rainfall, most literature on orographic precipitation has focused on the midlatitudes

[e.g., see reviews by Banta (1990), Roe (2005), Smith (2006), and Rotunno and Houze (2007)].

Recent work has begun to examine orographically modified tropical precipitation in more detail, largely focusing on rainfall from diurnally forced deep convection and tropical cyclones [e.g., see review by Houze (2012)]. Where strong and moist tropical flow encounters topography, shallow convection mechanically forced by orographic ascent can also produce significant rainfall. This phenomenon has received less study, even though it can play a dominant role in shaping the hydroclimate of certain regions (e.g., Rasmussen et al. 1989; Smith et al. 2009). The exception is a series of studies over the island of Hawaii. When strong moist trade winds are lifted over the Hawaiian terrain, shallow cumuli form or are enhanced, but are prevented from growing deep by the trade wind inversion. However, the large size of Hawaii complicates the study of this rainfall enhancement since upwind blocking diverts much of the flow around the island and triggers rainfall over the ocean (e.g., Rasmussen et al. 1989) and diurnal heating of the landmass leads to slope and land-sea circulations that modify the convection and rainfall (e.g., Chen and Nash 1994; Carbone et al. 1995).

* Supplemental information related to this paper is available at the Journals Online website: <http://dx.doi.org/10.1175/JAS-D-13-016.s1>.

Corresponding author address: Justin R. Minder, Department of Atmospheric and Environmental Sciences, University at Albany, State University of New York, 1400 Washington Avenue, Albany, NY 12222.
E-mail: justinminder@gmail.com

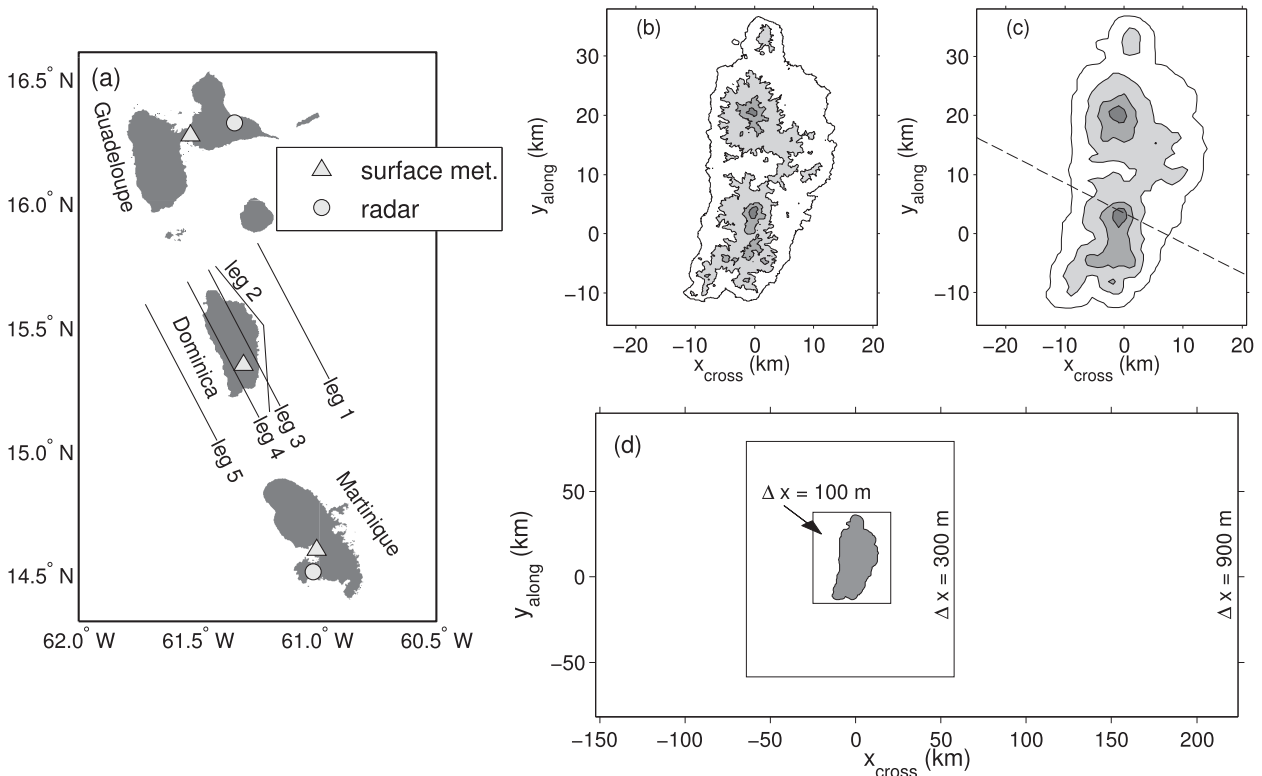


FIG. 1. Geography and topography of the study region. (a) The island of Dominica, neighboring islands, the location of surface meteorological stations and Meteo France radars discussed in the text, and the UWKA's flight tracks. (b) The topography of Dominica (from the Shuttle Radar Topography Mission) contoured every 400 m. (c) The smoothed version of the Dominican topography used in WRF simulations. (d) The domain configuration and horizontal grid spacing used for WRF simulations. Plots (b)–(d) are shown in a terrain-relative coordinate system that is aligned with the UWKA's flight tracks. Dashed line in (c) is the location of the section shown in Figs. 10 and 11.

In the midlatitudes, mesoscale airflow dynamics strongly shape the distribution and intensity of orographic rainfall through gravity waves, terrain blocking, localized convergence, convective triggering, etc. (e.g., Banta 1990; Roe 2005; Smith 2006; Rotunno and Houze 2007; Houze 2012). Furthermore, latent heating associated with condensation and precipitation from orographic clouds feeds back onto airflow dynamics (Smith and Lin 1982; Durran and Klemp 1983; Jiang 2003). In the tropics, we expect the interactions between mesoscale airflow dynamics and orographic precipitation to be similarly strong. But, the character of these interactions is likely distinct owing to 1) the large moisture contents found in the tropics that impact dynamics directly (through molecular weight effects) and indirectly (through latent heat release during condensation), 2) the typical conditionally unstable atmospheric stratification that leads to convection under most scenarios of orographic uplift and rainfall, and 3) strong subsidence inversions associated with subtropical highs that can strongly modify orographic airflow and suppress convective growth. This study will investigate the

dynamics of orographic convection in the tropics using the island of Dominica as a case study.

a. The DOMEX field campaign

The Caribbean island of Dominica (15°25'N, 61°21'W; Figs. 1a,b) offers a natural laboratory to study ascent-forced orographic convection and rainfall in the tropics. Studies of dynamics and convection are facilitated by the island's modest height (peak elevation 1.45 km), simple terrain geometry (Fig. 1b), and by persistent moist trade winds that produce frequent orographic showers. Annual rainfall over the high terrain can exceed 5 m, representing an orographic enhancement of about 3–5 times the upwind overocean rainfall (Smith et al. 2009). The lack of a discernible diurnal cycle in rainfall over the island indicates that orographic enhancement of convection and rainfall is not primarily forced by solar heating of the terrain but rather by mechanical lifting of the trade wind flow (Smith et al. 2009).

Convective-scale mechanisms for enhancement of convection and rainfall by orographic lifting have been

investigated with both theory and numerical simulations. Enhancement appears to occur because of 1) increased cloud fraction in the orographically lifted air, 2) buoyancy variations generated by bulk lifting of a horizontally inhomogeneous layer (Kirshbaum and Smith 2009), and 3) the occurrence of larger clouds with less entrainment over the terrain relative to the ocean (Kirshbaum and Grant 2012).

The mesoscale dynamics of airflow over Dominica have not been investigated in depth. Smith et al. (2009) used scale analysis and shallow water theory to suggest that flow over Dominica should undergo a subcritical-to-supercritical transition, leading to plunging flow and turbulent dissipation over the lee slopes. However, this analysis neglected the effects of latent heating and realistic vertical profiles. Kirshbaum and Smith (2009)'s simulations show evidence of plunging flow leading to turbulent vertical mixing. However, their simulations did not account for the three-dimensional terrain geometry and they did not examine the downslope flow, or its effects on the wake, in detail.

Detailed observations of airflow and clouds over Dominica took place during the Dominica Experiment 2011 (DOMEX-2011) campaign (Smith et al. 2012). This field experiment included 21 missions flown by the University of Wyoming King Air (UWKA; www.atmos.uwyo.edu/n2uw/), collecting in situ measurements of winds, thermodynamics, and microphysical properties as well as remote sensing of aerosol, cloud, and precipitation from an onboard lidar and cloud radar. Missions were flown on days without large-scale disturbances to focus on purely orographic effects, and followed fixed flight tracks (Fig. 1a) to allow for clear comparisons between cases. Surface observations and time-lapse photography were also collected.

Initial results from DOMEX-2011 indicate that the strength of the trade wind exerts a strong control on the nature of convection and rainfall over Dominica. Under weak trades ($<5 \text{ m s}^{-1}$), solar heating of the terrain drives thermally forced convection, producing strong updrafts and lofting island-derived tracers but leading to minimal rainfall. Under strong trades ($>8 \text{ m s}^{-1}$), mechanical lifting by the terrain drives ascent-forced convection with heavy rainfall, a dry and turbulent plunging flow, and a wake of decelerated air, enriched in island-derived tracers.

b. Overview

The present study provides a detailed analysis of the mesoscale dynamics of ascent-forced convection over Dominica under strong trade winds. Such conditions appear to produce the majority of rainfall over Dominica. Section 2 describes the observational datasets and

modeling system used. Section 3 gives an overview of a specific day during DOMEX which will be the focus of this study. Sections 4–6 examine the dynamics of upwind flow deformation, overisland convection and plunging flow, and downwind air mass transformation. Section 7 uses numerical sensitivity experiments to isolate the roles of latent heating and overisland drag in shaping airflow dynamics. Results are summarized in section 8.

2. Methods

This study examines the conditions corresponding to a specific DOMEX research flight (RF) through synthesis of airborne in situ observations and output from numerical modeling.

a. Observations

Airborne observations were made during research flight 13 (RF13): a 4-h flight of the UWKA on 27 April 2011. The flight consisted of an upstream sounding (from 4 km to 150 m) followed by horizontal legs along five tracks (Fig. 1a). Legs 1, 2, and 5 were flown over the ocean at two altitudes: high (H, 1.2 km) and low (L, 300 m). Legs 3 and 4 were flown at a higher altitude of 1.7 km to maintain adequate terrain clearance. The sequence of legs was sounding, 1L, 2L, 1H, 2H, 3, 4, 3, 4, 5L, and 5H.

This study uses in situ dynamical and thermodynamical variables sampled during the flight. A summary of relevant variables and instruments is given in Table 1. All results presented are from data sampled at 1 Hz (approximately 100-m along-track sampling), with the exception of turbulent kinetic energy (TKE). Using 25-Hz data, perturbations of wind fields u , v , and w from a slowly varying mean are produced and used to calculate TKE. Perturbations are produced by a high-pass ninth-order Butterworth filter with a 0.02-Hz cutoff frequency. The TKE is then smoothed to reduce sampling noise (using a low-pass ninth-order Butterworth filter with a 0.08-Hz cutoff). To facilitate the characterization of horizontal pressure gradients that drive mesoscale circulations, an equivalent constant-height “mesoscale” pressure p_m field is calculated by removing the effects of along-track vertical displacements of the aircraft and synoptic-scale pressure variations from the aircraft-measured static pressure (see appendix for details). Additionally, remote observations of clouds and precipitation were made using the onboard 95-GHz Wyoming Cloud Radar (WCR; www.atmos.uwyo.edu/wcr/).

Regional cloud fields were characterized using Geostationary Operational Environmental Satellite East (GOES-East) visible imagery. Hourly precipitation maps were

TABLE 1. UWKA in situ instrumentation and variables measured.

Variable	Instruments
Position (x, y, z)	Inertial Navigation System (INS) corrected with GPS ^a
3D winds (u, v, w)	Gust probe with INS
Static temperature (T)	Reverse-flow thermometer ^b
Static pressure (p)	Rosemount 1501 with INS
Water vapor mixing ratio (q_v)	LICOR-6262 infrared gas analyzer
Liquid water mixing ratio (q_l)	Sum of Forward-Scattering Spectrometer Probe (FSSP) and two-dimensional optical array precipitation probe (2DP) droplet spectra
Turbulent kinetic energy (TKE)	Calculated from filtered $u, v,$ and w
“Mesoscale” pressure (p_m)	Calculated from $p, z,$ and station data ^c

^aGPS data are differentially corrected using base station on Martinique.

^bCorrected for evaporative cooling biases following Wang and Geerts (2009).

^cMethods described in appendix.

produced from Meteo France’s operational radars located on Guadeloupe and Martinique (Fig. 1a) using the methods of Tabary (2007) and Tabary et al. (2007). Estimates from the two radars were combined to minimize precipitation underestimation due to beam blockage. Surface rainfall was also measured directly with a network of data-logging tipping-bucket rain gauges (Smith et al. 2012).

b. Modeling

A high-resolution numerical simulation of the RF13 case is conducted using version 3.2.1 of the Weather Research and Forecasting Model (WRF; Skamarock et al. 2008). WRF is a fully compressible nonhydrostatic mesoscale model on a mass-based terrain-following grid. Output from the simulation is used to provide a detailed view of the mesoscale airflow and convection during this case and to conduct sensitivity experiments to isolate the role of specific physical processes.

The model domain consists of three interactively nested grids with horizontal grid spacing of 900, 300, and 100 m centered on a smoothed version of the Dominican topography. A rotated horizontal coordinate is used to align the model grid axes with the flight tracks and terrain (Fig. 1c). On the innermost domain, the terrain is about 140 grid points wide. Each grid has 131 vertical levels with vertical grid spacing of 55 m near the surface, increasing gradually with height. At these grid spacings, the large energy-containing eddies associated with cumulus convection and turbulent downslope winds are fairly well resolved (Bryan et al. 2003; Epifanio and Qian 2008).

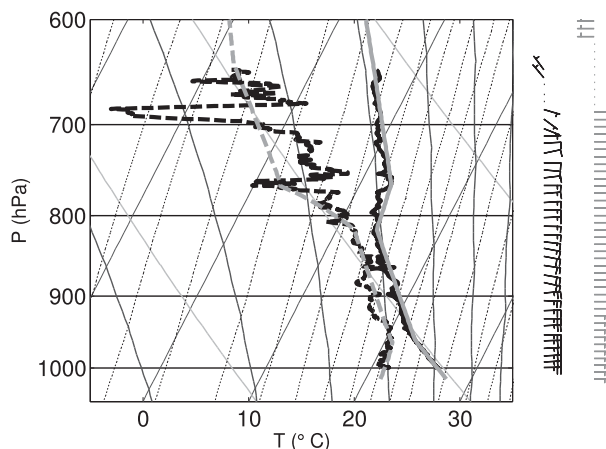


FIG. 2. Upwind sounding for RF13. Black lines show temperature (solid) and dewpoint (dashed) from UWKA sounding. Black wind barbs show the wind speed and direction (full barb = 5 m s^{-1}). Gray lines and barbs show the lower portion of the idealized RF13 sounding used to initialize the WRF simulation.

The bottom boundary conditions include no surface heat or moisture fluxes since we hypothesize that these do not play a major role in directly controlling the mesoscale airflow over the island. Surface drag is parameterized with the Eta surface layer scheme (Janjic 1996), based on Monin–Obukhov theory. Surface drag over Dominica is calculated using a roughness length of 0.8 m, while over the ocean a wind speed-dependent roughness is used. Subgrid-scale turbulence is parameterized using a 1.5-order TKE-based closure. Since the large energy-containing eddies are presumed to be explicitly resolved at these scales, no boundary layer parameterization is employed.

The model is initialized using an idealized version of the observed sounding from RF13, which is designed to match the aircraft sounding below 4 km and has uniform stratification and winds above (Fig. 2). A 1D simulation is run first in order to develop an initial condition with a three-way balance between pressure gradients, Coriolis, and surface drag in the PBL [following, e.g., Kirshbaum and Smith (2008)]. The domain of this preliminary simulation is only two grid points wide in x and y with periodic boundary conditions. Its output is used as a horizontally uniform initial condition for the 3D simulation.

The outer domain employs a periodic lateral boundary condition. On the upwind boundary there is a 30-gridpoint-wide damping region that linearly relaxes the incoming winds, potential temperature, and moisture fields back toward the initial vertical sounding. The upper boundary condition is a constant pressure surface, with the vertical velocity damping layer described by Klemp et al. (2008) applied above about 9.5 km MSL.

Our simulation approach differs from that of Kirshbaum and Smith (2008) and other large-eddy simulations (LES) of shallow cumuli. In neglecting surface heat and moisture fluxes we do not attempt to explicitly resolve turbulence and convection over the ocean (allowing a smaller and more affordable domain size for the 100-m grid). Instead we focus on explicitly resolving the effects of turbulence that is generated by airflow over Dominica. Although our simulations lack realistic upwind turbulence, its effects on the mean state are implicitly included in the observed sounding used for the initial condition and upwind boundary condition. We hypothesize that including these bulk effects of upwind turbulence is sufficient for capturing the near-island dynamics.

The Coriolis force is included using an f -plane approximation with $f = 3.9 \times 10^{-5} \text{ s}^{-1}$. No representation of atmospheric radiative fluxes, large-scale subsidence, or large-scale advection is included. Third-order Runge–Kutta time stepping is used, with fifth-order horizontal and third-order vertical advection. A positive-definite limiter is applied during the advection of microphysical variables and TKE (Skamarock and Weisman 2009). Additionally, a monotonic sixth-order filter (Knievel et al. 2007) is applied to damp out grid-scale variability.

Cloud and precipitation microphysics are parameterized using the two-moment bulk scheme of Milbrandt and Yau (2005). Within this, the activation of aerosols to form cloud droplets is calculated as a function of maximum supersaturation following the methods of Cohard et al. (1998) and Cohard and Pinty (2000). A uniform background aerosol field is assumed, composed of NaCl with a concentration of 66.6 cm^{-3} and a mean radius of $0.133 \text{ }\mu\text{m}$ (values corresponding to a default option for maritime conditions in the scheme).

To aid the development of a realistic field of cellular convection, small-amplitude perturbations are added to the flow near the upwind boundary of each domain. These take the form of random uncorrelated Gaussian-distributed perturbations added to q_v and θ fields over the lowest 40 model levels. Perturbations in q_v range between $\pm 2.5\%$ of the value of q_v . The θ perturbations are based on the q_v perturbations, such that the upwind buoyancy perturbations are approximately zero, motivated by the observations of Smith et al. (2012).

The model is run for 12.5 h. Model output, with 5-min frequency, is analyzed beginning at $t = 6.5 \text{ h}$, when most fields have reached a statistical steady state. Total TKE is calculated using perturbations from time-mean values to calculate a resolved component, which is then added to a parameterized component produced by the subgrid-scale turbulence scheme. Over and downwind of Dominica the resolved TKE is about 10 times larger than the

parameterized, suggesting that our simulations are effectively resolving the large energy-containing eddies.

3. Case overview

a. Observations

The focus of this study is 27 April 2011 (RF13) during the DOMEX field campaign. RF13 was flown from 1341 to 1738 UTC [0941–1338 Atlantic standard time (AST)]. This day was characteristic of days with strong trade winds, weak overisland diurnal surface temperature variations, and ascent-forced orographic convection during DOMEX (Smith et al. 2012). The upwind UWKA sounding (Fig. 2) shows strong easterly trade winds ($>12 \text{ m s}^{-1}$) below 1 km. These winds weaken with height and reverse to westerly at about 3.5 km. This wind-reversal height represents a critical level h_c for upward-propagating gravity waves launched by flow over Dominica. Thermodynamic variables show a well-mixed subcloud layer (0–0.5 km), a moist and conditionally unstable cloud layer (0.5–2 km), an “inversion layer” with strong stability and decreasing moisture (2–2.5 km), and dry air with nearly moist-neutral conditions aloft. This vertical structure is typical of the Atlantic trade wind regime (e.g., Holland and Rasmusson 1973; Rauber et al. 2007).

Some relevant parameters from the RF13 sounding and terrain geometry are summarized in Table 2. The analysis of Smith (1989) provides a regime diagram that predicts the character of hydrostatic, uniform, inviscid, dry, three-dimensional, stratified flow over topography as a function of the terrain’s horizontal aspect ratio r and nondimensional mountain height ($h_m N/U$). For RF13, depending on the choice of parameters in Table 2, Smith (1989)’s theory predicts the flow to be either in a gravity wave breaking regime (with flow stagnation above the mountain crest) or in a regime characterized by both flow splitting (with flow stagnation on the mountain’s windward slopes) and wave breaking. Unfortunately, the application of this theory to the RF13 case is highly uncertain owing to the violation of several assumptions. For instance, the nonuniform vertical wind profile has significant reverse shear, which would tend to favor wave breaking aloft over flow splitting (Smith 1989). Latent heating due to condensation of clouds over the terrain should generally act to reduce both flow splitting and gravity wave amplitude (e.g., Durran and Klemp 1983; Jiang 2003). These and other complications (e.g., convective instability, surface heat fluxes) mean that analytical theory can only provide us with general expectations for this case.

A representative visible satellite image from RF13 is shown in Fig. 3a from 1638 UTC. A field of scattered

TABLE 2. Terrain and RF13 sounding parameters relevant to nondimensional analysis. Low-level sounding parameters (U , N , and N_m^2) are calculated for two different layers (200–1800 and 200–3000 m) to give a range of values. A range of values is also given for the terrain height h_m because of the complexity of the topography.

Symbol	Parameter	Value
U	Cross-mountain wind speed	6.9–9.4 m s ⁻¹
N	Brunt–Väisälä frequency (dry)	0.0083–0.011 s ⁻¹
N_m^2	Moist Brunt–Väisälä frequency squared	-1.4 to -0.6 × 10 ⁻⁴ s ⁻²
h_m	Terrain height	800–1200 m
h_c	Critical-level height	3.5 km
r	Terrain horizontal aspect ratio	~2.5
$h_m N/U$	Nondimensional mountain height	0.71–1.91
$h_c N/U$	Nondimensional critical-level height	3.1–5.6
$F_{o,zonal}$	Vertically integrated vapor flux (zonal)	368.9 kg m ⁻¹ s ⁻¹
$F_{o,cross\ mtn}$	Vertically integrated vapor flux (cross mountain)	327.9 kg m ⁻¹ s ⁻¹
P_{tot}	Total rainfall per crosswind length (over box in Fig. 4a)	2.587 kg m ⁻¹ s ⁻¹
DR	Drying ratio ($P_{tot}/F_{o,zonal}$)	0.70%

trade wind cumuli is located upwind of Dominica, with some evidence of mesoscale organization into bands. Over the windward slope and the crest of Dominica, clouds are much more densely packed. Over the leeward slope, the clouds abruptly end and are suppressed in the wake region, except in two zonal convergence lines. Figure 3b shows reflectivity from the lowest unblocked beam (0° over the ocean, and higher over Dominica's peaks) at 1625 UTC. Only a few weak echoes are found upwind of Dominica, demonstrating that most of the upwind cumuli are not raining or only producing light rainfall. This contrasts with conditions over Dominica, where echoes upward of 35 dBZ_e indicate moderate to heavy rainfall. Time animations of radar, visible satellite, and on-island cloud photography (see supplemental material) reveal that passage of air over Dominica both initiates new raining convective cells and intensifies rainfall from existing cells (Smith et al. 2012). Furthermore, these animations show little diurnal modulation of the overisland convection, suggesting that forced ascent rather than solar heating controls initiation of overisland convection.

Daily mean rainfall rates measured by rain gauges and estimated by radar for 0000–2400 UTC 27 April 2011 are shown in Fig. 4a. These two datasets show good agreement regarding the cross-mountain variations in rainfall. Over the ocean, modest rain rates of around 0.2 mm h⁻¹ are found. Over the windward slopes, rainfall quickly increases to upward of 1.5 mm h⁻¹, with strong modulation of rainfall over the island's major peaks and saddle. Conditional rainfall intensity (calculated by averaging only 15-min periods with measured rainfall) is much higher than the mean values, reaching above 3.5 mm h⁻¹ at all but the coastal gauges (Fig. 4b), and rainfall frequency (calculated as the percentage of 15-min periods with measured rainfall) is at most 40%

(Fig. 4c). These small values are consistent with previous observations that most of Dominica's rainfall comes from short intense showers (Smith et al. 2009). There is little evidence of terrain-induced rainfall enhancement upwind of the Dominican coast. Downwind

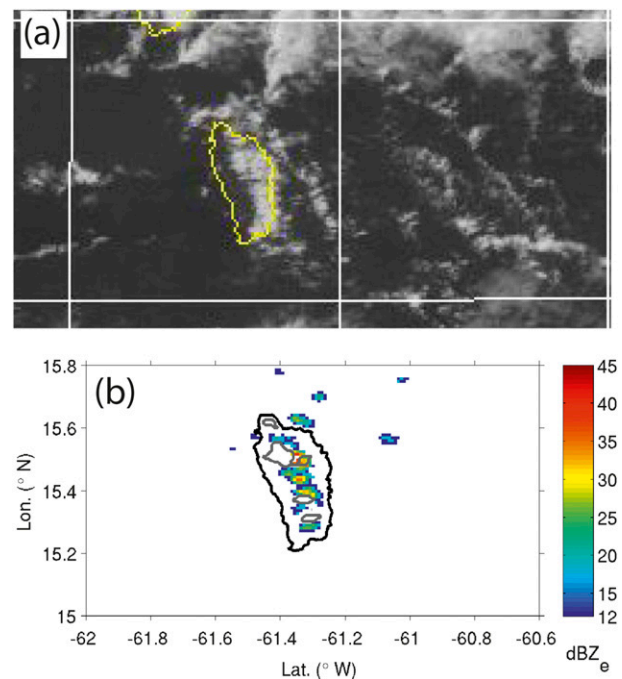


FIG. 3. (a) GOES-East visible image at 1638 UTC showing scattered trade wind cumuli upwind and densely packed cumuli over Dominica. (b) Low-level reflectivity from Meteo France's Guadeloupe radar at 1625 UTC showing moderate to heavy rainfall over Dominica's high terrain. Gray contours in (b) denote regions where elevation angles of 1.6° or 3.8° are used to avoid terrain. These regions often display no echo because the radar beam passes over the top of the shallow convection.

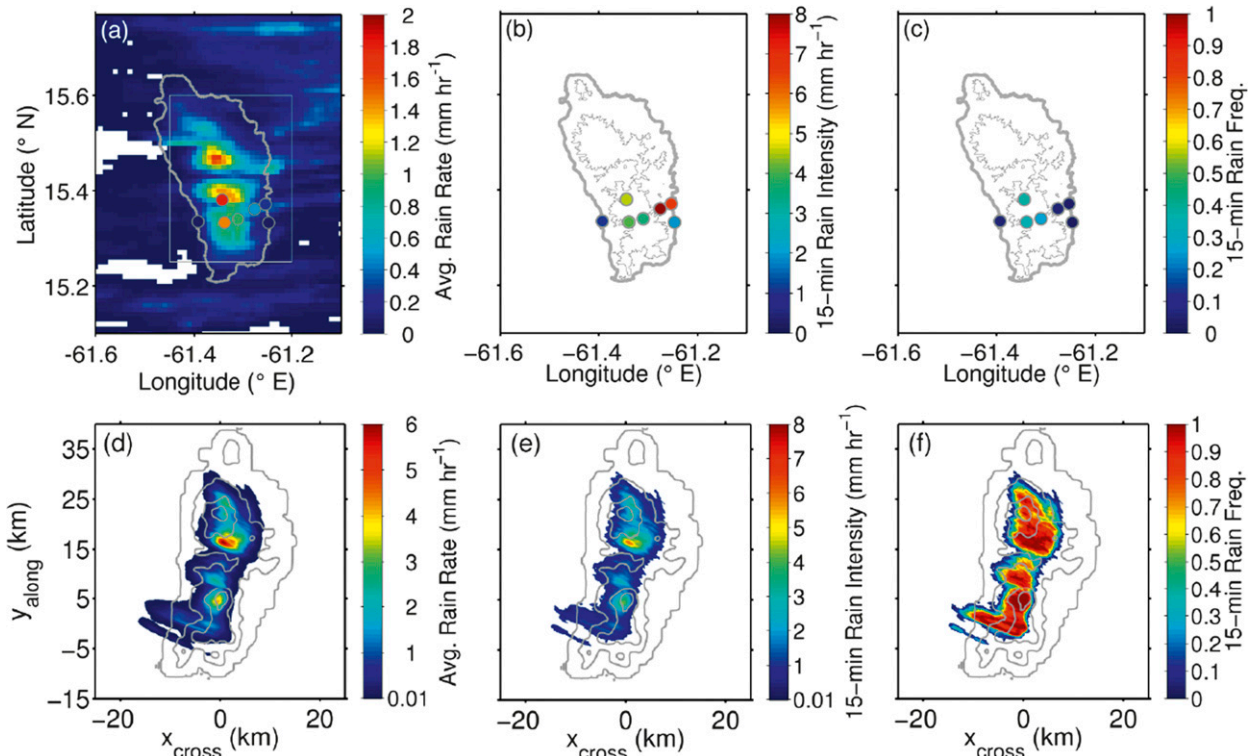


FIG. 4. Observed and simulated rainfall. (a) Average rainfall rate for 0000–2400 UTC 27 Feb 2011. Color shading shows estimate from Meteo France radars. Colored circles show observations from tipping-bucket gauges. Gray box shows region used for calculating DR statistics. (b) Observed conditionally averaged 15-min rainfall intensity (averaged only over raining periods) from gauges. (c) 15-min rainfall frequency observed from gauges. (d) Average rainfall rate from WRF simulation. (e) Conditionally averaged 15-min rainfall rate from WRF. (f) 15-min rainfall frequency from WRF.

of the terrain crest is an abrupt decrease in rainfall, with apparently suppressed rainfall in the wake.

A fundamental measure of the efficacy of orographic precipitation is the drying ratio (DR), which compares the amount of precipitation induced by a barrier P_{tot} to the incoming flux of water vapor by the mean wind F_o . Integrating the daily mean rainfall rates over the gray box in Fig. 4a and dividing by the box's meridional extent yields $P_{\text{tot}} = 2.587 \text{ kg m}^{-1} \text{ s}^{-1}$. Integrating the zonal flux of water vapor (from the UWKA's sounding) from the surface to h_c yields $F_{o,\text{zonal}} = 368.9 \text{ kg m}^{-1} \text{ s}^{-1}$. Combining these gives a daily averaged $\text{DR} = P_{\text{tot}}/F_{o,\text{zonal}} = 0.70\%$. This is consistent with earlier estimates based on observations (Smith et al. 2009) and large-eddy simulations (Kirshbaum and Smith 2009) that estimated DR's close to 1% for Dominica.

Winds measured by the UWKA are plotted in Fig. 5. Upwind of the island (leg 1) the winds are strong, easterly, and uniform. Along the windward coast (leg 2) there is evidence for modest terrain-induced flow deceleration and flow deflection, with somewhat reduced winds near the island's center, accelerated winds near the ends of the island, and modest diffuence. Over the

windward slopes (leg 3) easterly winds are maintained. However, over the lee slopes (leg 4) winds become much more weak and variable in the regions directly downwind of the high terrain. Downwind of the island (leg 5) a distinct wake is present, particularly at low levels, with winds strongly decelerated relative to upwind conditions. Outside of the wake the winds are accelerated.

b. Modeling

Figure 6 shows a 3D rendering of instantaneous simulated cloud and rain fields. Consistent with the satellite imagery (Fig. 3), closely packed convection is found over the windward slopes of Dominica, starting very near to the coastline (Fig. 6a). Before these clouds reach the island's crest they produce rain shafts. In the lee, the clouds dissipate abruptly, but some rainfall spills over to the lee coast (Fig. 6b).

These features are reflected in the modeled surface rainfall rates (Fig. 4d), which show heavy rainfall over the high terrain, no rain on the upwind coast, and only a small region of spillover rain in the lee. By design, the simulation has no upwind rainfall, since surface fluxes to force convection over the ocean are not included.

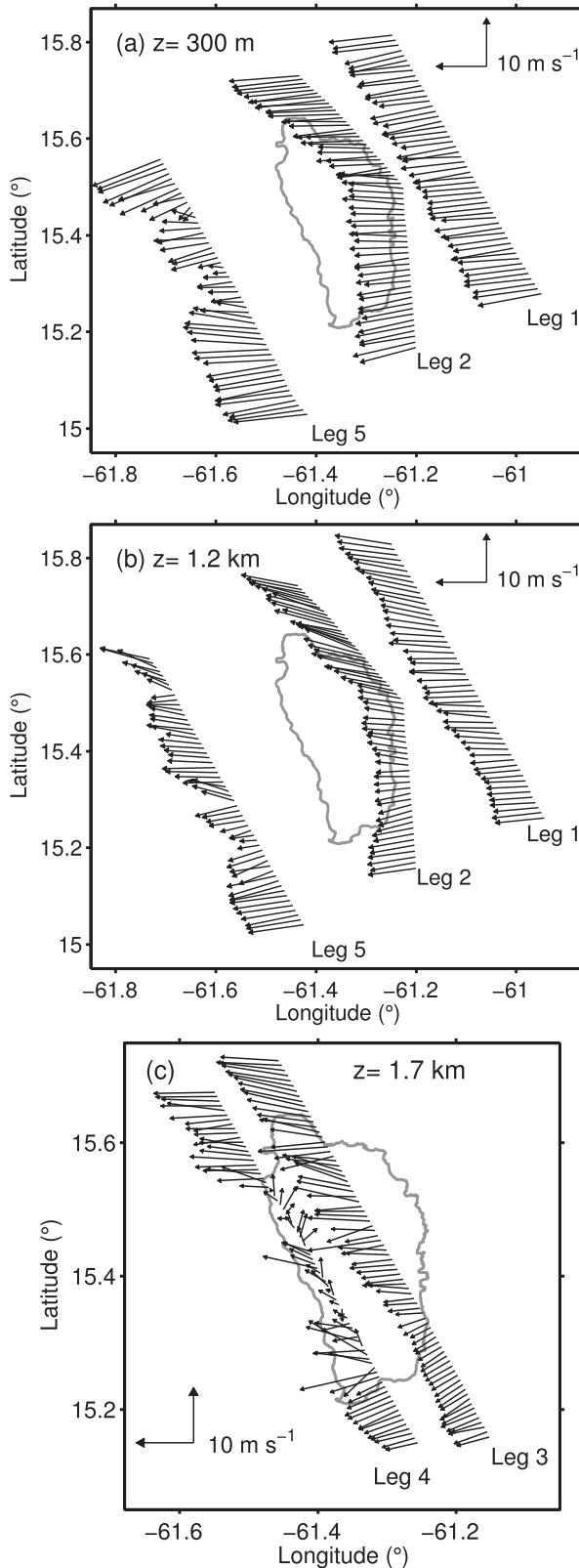


FIG. 5. Flight-level horizontal winds measured by UWKA during RF13: (a) low legs ($z = 300$ m MSL), (b) high legs ($z = 1.2$ km MSL), and (c) convection legs ($z = 1.7$ km MSL). Vectors are plotted every 15 s (~ 1.5 km) in (a),(b) and every 10 s (~ 1 km) in (c).

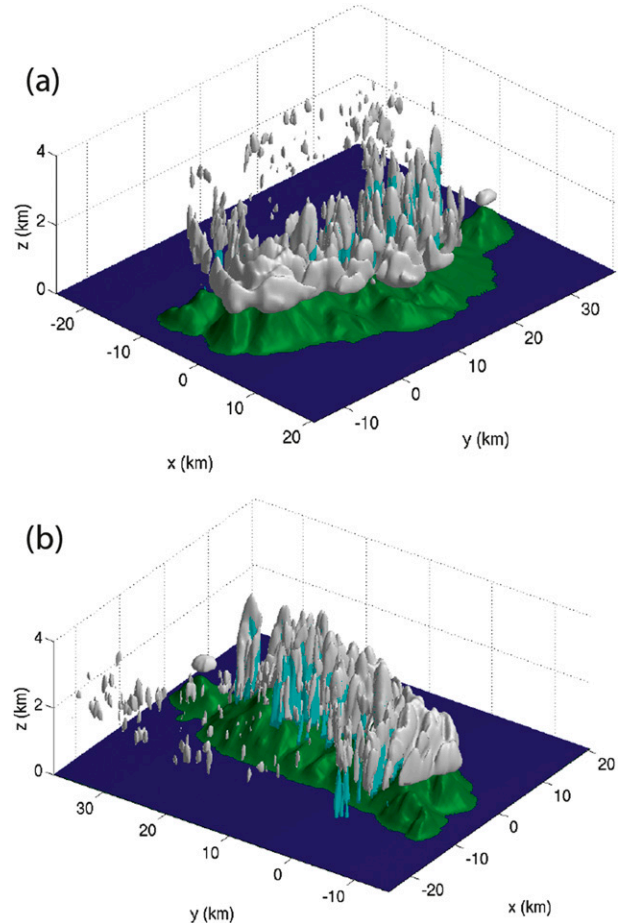


FIG. 6. Cloud and rain from WRF simulation of RF13 at $t = 6.5$ h. Isosurfaces of cloud water mixing ratio are shown in gray ($q_c = 0.2 \text{ g kg}^{-1}$), and isosurfaces of rainwater mixing ratio are shown in cyan ($q_r = 0.02 \text{ g kg}^{-1}$). (a),(b) Same isosurfaces from different viewing aspects.

Simulated rainfall over the high terrain broadly agrees with observations in terms of spatial structure. However, spatial-maximum rainfall rates in the simulation are more localized and as much as 3 times higher than observed. This is partially due to excessive frequency of rainfall over the high terrain (Fig. 4f), which leads to excessive rainfall despite rain intensities that are close to observed (Fig. 4e). These differences could arise from biases in the model's microphysical parameterization or deficiencies in the upwind flow specification (such as the lack of an upwind cloud field). Despite these biases, the island-averaged rainfall is similar. Integrating over the rainfall field in Fig. 4b and comparing to the upwind cross-mountain flux, we find a simulated cross-mountain DR = 0.68%, which is close to the observed zonal DR presented above (differences between cross-mountain and zonal fluxes barely change the DR).

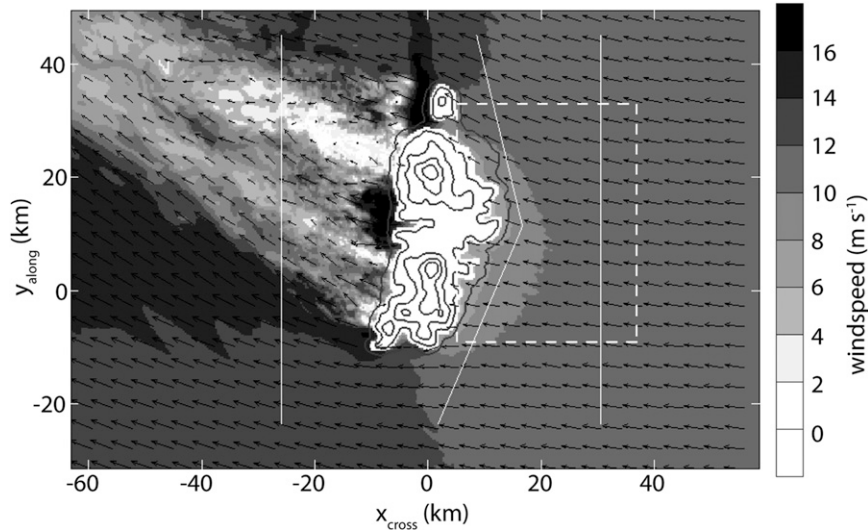


FIG. 7. Winds at 300 m from WRF simulation (intermediate domain, $\Delta x = 300$ m). Vectors show horizontal winds. Shading shows horizontal wind speed according to scale bar. The dashed box corresponds to control volume used for blocking-ratio calculation. The thin solid lines correspond to the approximate location of UWKA legs 1, 2, and 5.

Figure 7 reveals that the basic observed pattern of low-level airflow is reproduced by WRF. At 300 m there is only moderate deflection and deceleration of the flow upwind of Dominica. In the lee there is a distinct wake of decelerated flow showing subwake structures associated with the individual peaks and saddles of the terrain. Outside of the wake the downwind flow is significantly accelerated.

The following three sections use both observations and WRF output to examine the mesoscale dynamics of this case in detail, focusing on three separate issues: 1) upwind flow deformation, 2) overisland windward convection and leeward plunging flow, and 3) the downwind wake.

4. Upwind flow deformation

Upwind orographic modification of airflow is important, since it can produce upwind convergence and convective initiation (e.g., Rasmussen et al. 1989; Carbone et al. 1998) or blocking and diversion of water vapor around the terrain (e.g., Jiang 2003; Galewsky 2008).

a. Observations

Selected dynamical variables observed on legs 1L and 2L are shown in Figs. 8a–d. Figures 8a–c show the mesoscale pressure p_m (described in the appendix) and terrain-relative winds (u_{cross} and v_{along}). Far upwind of the terrain on leg 1L these variables show little mesoscale variation, only microscale variation associated with

boundary layer turbulence. Along the coast, on leg 2L, there is a slight increase in p_m near the center of the island. On the ends of leg 2L, near the island's tips, there are larger drops in p_m . These pressure anomalies are likely generated by vertical displacements of the stratified trade wind flow. Lifting upwind of the center of the island produces a cold anomaly aloft and—by hydrostatic balance—increased p_m at flight level. The lack of substantial lifting and pressure perturbation upwind of the island's center is consistent with the lack of evidence for upwind convective triggering and precipitation enhancement in the satellite and radar data. Similarly, descent near the island's ends can explain the lower p_m found there.

Winds along the coast also show signs of orographic modification. The magnitude of u_{cross} is decreased along much of the Dominican coast and increased near the north-northwestern end, while v_{along} is decreased near the south-southeastern end and increased in the north-northwest. Thus, the flow is slowing and diverting around the island, but there is no evidence for flow stagnation or splitting. This disagrees with Smith (1989)'s regime diagram, which predicts the flow should be near the threshold for flow spitting. Possible reasons for the minimal flow deflection include 1) reduced effective stratification and upwind pressure anomalies due to overisland latent heating (Smith and Lin 1982; Jiang and Smith 2003), 2) dynamical effects of sensible heating over the sunwarmed terrain (Reisner and Smolarkiewicz 1994), and 3) the lack of stratification in the lowest 600 m of the sounding.

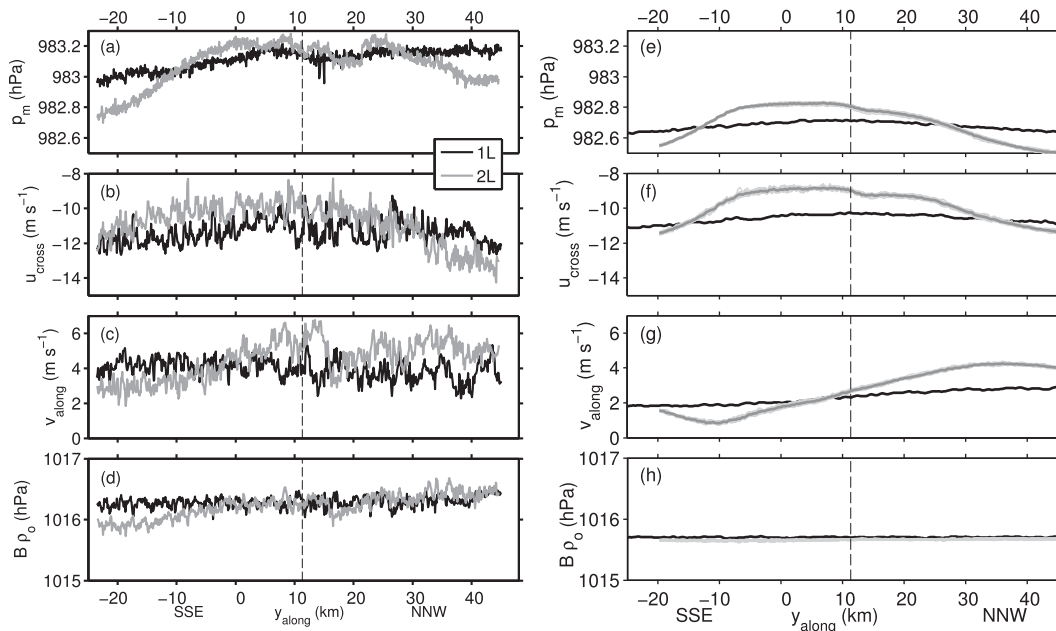


FIG. 8. Select dynamical variables along upwind legs 1L and 2L (300 m MSL). (a)–(d) Observed p_m , u_{cross} , v_{along} , and $B\rho_o$. (e)–(h) As in (a)–(d), respectively, but from intermediate WRF domain ($\Delta x = 300$ m). For leg 2L, individual lines are plotted every 5 min over 2 h (light gray) and the time mean is plotted (dark gray). Vertical dashed line shows the location of the turn on leg 2.

Insight into the dynamical relationship between the pressure and wind anomalies can be gained by analysis of a Bernoulli function B . Here we consider an incompressible version:

$$B = \frac{p_m}{\rho_o} + gz_{\text{leg}} + \frac{1}{2}(u_{\text{cross}}^2 + v_{\text{along}}^2), \quad (1)$$

where $\rho_o = 1.1 \text{ g kg}^{-1}$. The nominal height of a flight leg z_{leg} (here 300 m) is used because variations about that altitude are already incorporated into p_m (see the appendix). If the flow is inviscid, steady, incompressible, and adiabatic, then B will be conserved following streamlines. If deviations from these assumptions are small, and the upwind low-level flow does not rise or sink substantially, conservation of B can relate the observed wind and pressure anomalies.

Figure 8d shows B (multiplied by ρ_o to give units comparable to p_m) for the upwind legs. North-northwest of $y_{\text{along}} = 0$, the value of B on legs 1L and 2L is very similar, suggesting that the observed pressure anomaly accounts for the deceleration of the flow near the center of the coast and the acceleration to the north-northwest. In contrast, on the south-southeastern end of leg 2L there is a substantial drop in B relative to the upwind, indicating that the flow acceleration on that end is less than would be expected from the p_m anomaly. The reason for this is unclear. It could be due to vertical

displacement of streamlines or convective momentum transport.

b. Modeling

Upwind low-leg dynamical variables from the WRF simulation are shown in Figs. 8e–h. Along leg 2L, the steadiness of the flow is revealed by plotting 3.5 h of 5-min output in addition to time-mean values. Simulated fields are smoother than the observed owing to the absence of surface heat and moisture fluxes to drive boundary layer turbulence. The p_m and wind fields show similar mesoscale structures along the coast to those observed. A positive p_m perturbation in the island's center is associated with ascent aloft, and negative perturbations on the ends are associated with descent. However, the positive perturbations are larger and the negative perturbations are less than observed. The trade wind flow slows and diverts around the island similarly to the observed flow. Since the present simulation did not include any overisland heat fluxes it appears that surface heating over the terrain is not the primary process preventing flow blocking. The conservation of B between legs 1L and 2L is much better than observed, indicating a tighter coupling between p_m and wind perturbations.

Three-dimensional gridded WRF output allows us to calculate how orographic flow deflection affects the moisture flux over the terrain—a calculation not possible with flight-level data alone. We consider an upwind

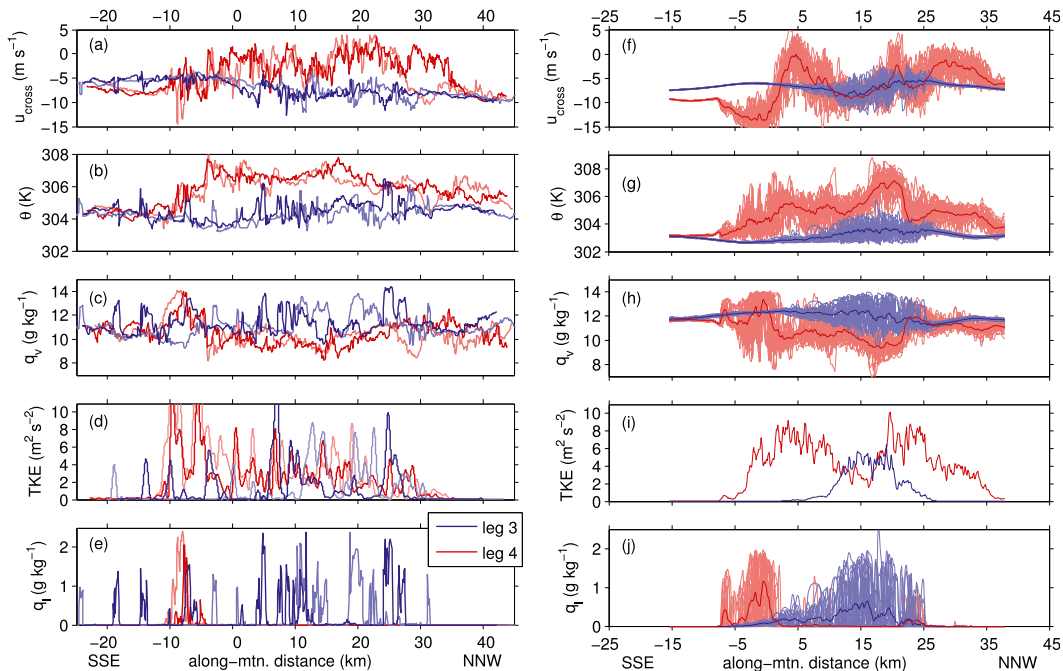


FIG. 9. Select dynamical variables along overisland legs 3 and 4 (1.7 km MSL). (a)–(e) Observed u_{cross} , θ , q_v , TKE, and q_l . These data are shown for two separate passes along these legs using light- and dark-colored lines to denote the separate passes. (f)–(j) As in (a)–(e), respectively, but from the innermost WRF domain ($\Delta x = 100$ m). In these data, light-colored lines show instantaneous values every 5 min over 2 h, whereas dark lines show the time mean.

control box shown in Fig. 7, extending through the bottom 50 model levels (the approximate depth of the easterly trade wind flow). The total horizontal flux of water vapor through each vertical face of the control volume is calculated every 5 min for 3.5 h and averaged. By comparing the cross-mountain flux through the upwind face with the net along-mountain fluxes through the two terrain-perpendicular faces we calculate a “blocking ratio”: $BR = (F_n - F_s)/(-F_{\text{up}})$ (where subscripts n , s , and up refer to northern, southern, and upwind faces). For this case $BR = 16\%$, revealing that the deflection of flow around the island has a small but nonnegligible effect on reducing the vapor available for orographic precipitation.

5. Overisland convection and plunging flow

Over Dominica, the terrain generates windward moist convection that brings heavy rainfall. However, it also generates a dry and turbulent leeside plunging flow that dissipates clouds and suppresses precipitation.

a. Observations

Figures 9a–e show flight-level data from two passes of the UWKA over legs 3 and 4. On leg 3, penetrations through convective clouds lead to elevated TKE, θ , q_v ,

and q_l . Vertical reflectivity profiles from the WCR show these convective plumes reach upward of 3.5 km (Smith et al. 2012). The air in the lee of the high terrain on leg 4 has very weak u_{cross} relative to that on leg 3 just upwind (also seen in Fig. 5c), which is possibly an indication that the strong trade wind flow has plunged beneath the flight level (e.g., Lilly 1978; Smith 1987; Smith et al. 1997). This air in the lee is also potentially warmer and drier. This thermodynamic signal could result from air that has either 1) descended from aloft in plunging flow or 2) experienced substantial latent heating and rainout during convection. While leg 4 is mostly free of clouds and rainfall (Fig. 9e), below the aircraft the WCR detects low-level echoes from rain that has spilled over into the lee, advected by the easterly winds (Smith et al. 2012).

Some statistical measures of the convection and turbulence encountered over the terrain are shown in Table 3. These are calculated separately for each of the repeated legs. As expected, the cloud fraction is substantially higher on leg 3, although it does not even reach 25% (cloud fractions appear larger in Fig. 3a owing to cloud-top detrainment). The strength of turbulent fluctuations (as measured by TKE) is on average stronger on leg 4. This is because turbulence on leg 3 is limited to the vicinity of convective updrafts, but is widespread in the lee of the terrain on leg 4.

TABLE 3. Selected cloud and turbulence statistics calculated over the near-island section of legs 3 and 4 ($y_{\text{along}} = -15.5$ – 37.9 km). Statistics from UWKA observations (Obs) are calculated and reported separately for each of the repeated legs. Statistics from the WRF simulation are calculated using 5-min output from $t = 6.5$ – 12.5 h, and then averaged along the legs.

Variable	Obs	WRF
Cloud fraction (%)		
Leg 3	15, 20	19.9
Leg 4	4.1, 5.6	9.1
TKE (m s^{-1})		
Leg 3	1.1, 1.3	0.99
Leg 4	2.8, 2.2	3.9
$\overline{w'^2}$		
2TKE		
Leg 3	0.41, 0.41	0.37
Leg 4	0.24, 0.28	0.29
$\overline{u'^2}$		
2TKE		
Leg 3	0.36, 0.27	0.30
Leg 4	0.47, 0.42	0.54

The character of the turbulence is also different on the two legs. Table 3 shows the contribution of w and u fluctuations to TKE ($\overline{w'^2}/2\text{TKE}$ and $\overline{u'^2}/2\text{TKE}$, respectively), providing a measure of the anisotropy of the turbulence (for isotropic turbulence these would each equal 0.33). On leg 3, the w' contribution to TKE is dominant, as is expected for turbulence recently generated by buoyancy forces. In contrast, on leg 4 the u' contribution is dominant, as expected for turbulence generated by shear instabilities produced by plunging downslope flow.

b. Modeling

Time-mean and instantaneous along-leg outputs from the innermost WRF domain are shown in Figs. 9f–j. Over the windward slopes, the simulated convection produces similar increases in θ , q_v , TKE, and q_i as measured by the UWKA. In the lee, deceleration, warming, and drying of the flow are simulated. Since the flow over the island is highly turbulent (note variability between individual WRF transects), it is difficult to compare the magnitude of this signal with the observations, but the observed leeside perturbations mostly fall within the envelope of the time-varying WRF output. On leg 3, the simulation only produces vigorous convection over the island north-northwest of about $y_{\text{along}} = 5$ km. Statistics from WRF output are shown in Table 3. The simulated windward cloud fraction is similar to the observed, and cloud fraction is reduced in the lee, but less strongly than observed. TKE is similar to the observed on leg 3 but is stronger than observed in the

lee. The observed contrasts in turbulence anisotropy between the two legs are reproduced.

In Fig. 10, we probe the structure of the simulated overisland flow by plotting along-wind vertical sections (location shown in Fig. 1c) at $t = 6.5$ h. In Fig. 10a, contours of θ_e provide approximate streamlines for the flow as it traverses Dominica, and shading shows u_{sec} . The θ_e lines do not begin to rise until just upwind of the windward coast, as expected from the minimal low-level p_m perturbation. As the trade winds are lifted over the terrain, convection develops, clouds form, and θ_e contours make large vertical excursions (Figs. 10a–c). Over the windward slopes there is little displacement of the inversion layer. Over the crest of the terrain, convection reaches above 3 km, penetrating into the inversion layer.

Over the lee slopes the flow has a very different character, with strong turbulent plunging flow (Fig. 10b) that effectively eliminates clouds and moist convection (Fig. 10c). In the lowest 500 m AGL there is a strong jet of downslope winds. This jet is capped by a region of nearly stagnant, turbulent air with weak vertical stratification of θ_e (Fig. 10a–b). On other research flights that include a cross-mountain leg, dual-Doppler analysis of WCR data below the aircraft provides evidence for this strong plunging flow.

Time-mean characteristics of the flow are shown in Fig. 11 by averaging the previous section over $t = 6.5$ – 12.5 h. The upwind convective plumes are removed by this averaging because of their sporadic nature. After averaging, the flow still shows little upwind ascent and a strong plunging lee jet, capped by stagnant air aloft (Fig. 11a). The mean fields also show downslope flow bringing dry air from aloft into the lee (Fig. 11b), explaining the low q_v found on leg 4. Large values of TKE are concentrated on the top of the leeside plunging jet (Fig. 11c), where TKE is likely generated by shear instability (Epifanio and Qian 2008; Smith and Skillingstad 2011). TKE produced by moist convection over the windward slopes is weak in the time mean because of its intermittent nature, although it is evident as a region of TKE dominated by w' (blue contour in Fig. 11c).

Figure 12 shows the three-dimensional distribution of turbulence over Dominica by plotting the isosurface of time-mean $\text{TKE} = 10 \text{ m}^2 \text{ s}^{-2}$. The primary regions of high TKE are found in the lee of Dominica's high terrain, where strong downslope winds drive shear instabilities. An additional, smaller, region is found aloft near the middle of the island, generated by the orographically triggered moist convection.

Several characteristics of the above-described airflow kinematics are reminiscent of those found in studies of downslope winds in stably stratified environments. The downslope plunge and turbulent rebound of streamlines

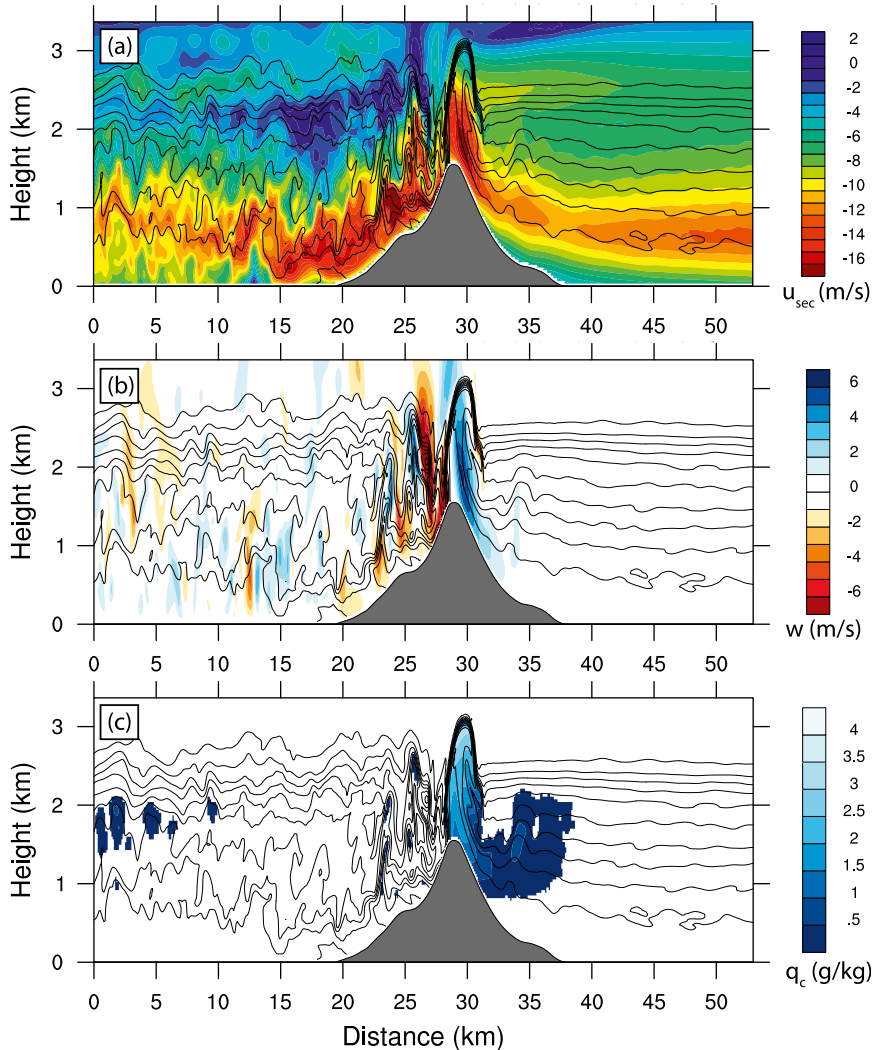


FIG. 10. Along-wind vertical sections through WRF output at 6.5 h (mean wind is from the right). Location of section is shown in Fig. 1c. All panels show θ_e with contours (every 2 K). (a) Along-section wind u_{sec} with color shading. (b) Vertical wind w with color shading. (c) Cloud water mixing ratio q_c with color shading.

are consistent with the subcritical to supercritical flow transition and hydraulic jumps found in continuously stratified analogs to hydraulic flow (Durrant 1986). The stagnant, well-mixed, turbulent air that caps the stratified plunging flow creates a critical layer for terrain-launched gravity waves. Such a flow morphology is dynamically favorable for strong plunging downslope winds (Smith 1985), and has been found in numerous downslope wind events (e.g., Lilly 1978; Smith 1987) and numerical simulations (e.g., Clark and Peltier 1984; Epifanio and Qian 2008; Smith and Skillingstad 2011). The presence of the inversion at 2.5 km and mean-state critical level at 3.5 km may play important roles in producing the strong downslope winds (Clark and Peltier 1984; Smith 1987; Sheridan and Vosper 2005;

Smith and Skillingstad 2011). However, the relatively large value of $h_m N/U$ for this case (Table 2) suggests that a self-induced critical layer from wave breaking may be the dominant factor forcing the strong plunging flow.

6. Downwind wake and airmass transformation

The wakes of Dominica and the other Lesser Antilles islands exhibit reduced low-level winds and suppressed clouds and rainfall tens to hundreds of kilometers downwind (Smith et al. 1997, 2009). Here, we characterize the dynamic and thermodynamic properties of Dominica's wake and identify the mechanisms that transform the upwind flow to have these properties.

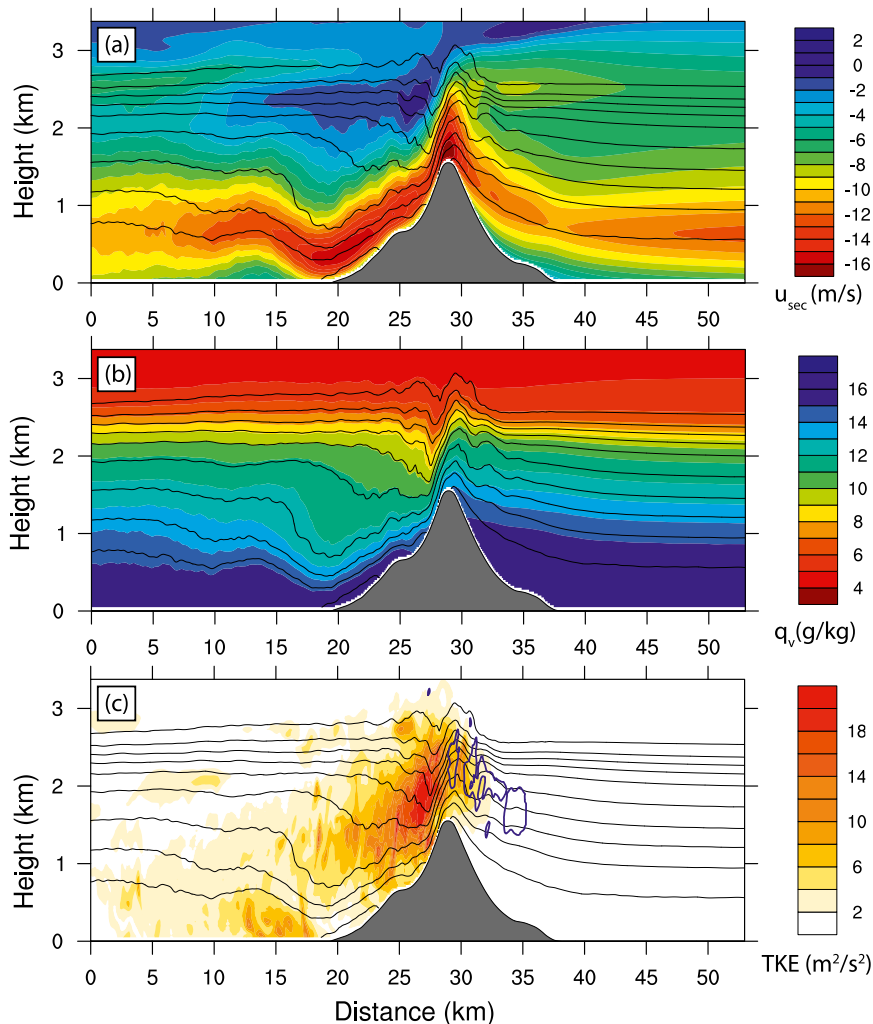


FIG. 11. Mean along-wind vertical sections through WRF output along the dashed line in Fig. 1c. Fields are averaged over 6 h (model hours 6.5–12.5, using 5-min output). All panels show θ_e with thin contours (every 2 K). (a) Mean u_{sec} with shading. (b) Mean q_v with shading. (c) Mean TKE with shading, and regions of w' -dominated TKE with contours of $0.5\sigma_w^2/\text{TKE} = 0.5$ (blue).

a. Observations

Flight-level data from UWKA legs 1L and 5L are shown in Fig. 13a–f. All variables except p_m show distinct wake signatures on leg 5L downwind of the terrain ($y_{\text{along}} \sim 0\text{--}35$ km). On leg 5L, the magnitude of u_{cross} is strongly reduced in the wake and somewhat increased outside of the wake (as seen in Fig. 5a). Distinct subwake structure is evident, with air in the lee of the high topography showing strong deceleration, while air downwind of Dominica's saddle is only weakly decelerated. This subwake structure is consistent with modeling and observational studies (e.g., Smith et al. 1997; Pan and Smith 1999; Gaberseck and Durran 2004). A uniform drop in p_m is found downwind of Dominica, as expected

owing to mountain wave descent aloft. The lack of any wake signature in p_m suggests that, at the distance of leg 5L, the low-level flow in the wake has equilibrated to remove any pressure gradients that may have been present in the plunging downslope flow.

To gain insight into the dynamical origin of the wake, we plot B in Fig. 13c, which should be conserved along streamlines if the flow is inviscid and adiabatic. Everywhere on leg 5L, B is reduced relative to leg 1L, and this reduction is enhanced in the wake. The in-wake reduction could be due to turbulent dissipation of momentum or vertical transport of B . Wake formation by turbulent dissipation in the plunging flow would be consistent with the results of Schar and Smith (1993), Smith et al. (1997), and Gaberseck and Durran (2004).

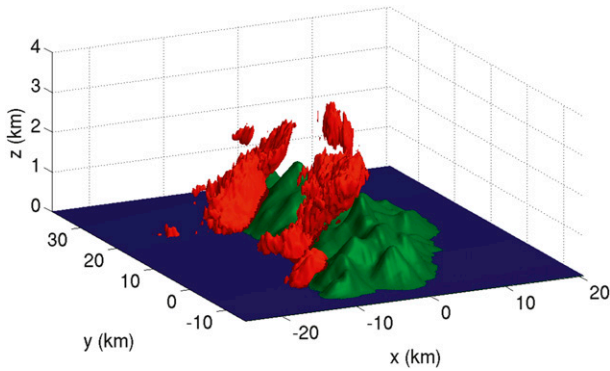


FIG. 12. Isosurfaces of time-mean $TKE = 10\text{ m}^{-2}\text{ s}^{-2}$ over Dominica (innermost domain, $\Delta x = 100\text{ m}$, calculated from $t = 6.5\text{--}12.5\text{ h}$).

Turbulent modification of B could be generated by surface drag over the island, by moist convection, or by the dry plunging flow. The cause of the reduction in B outside of the wake on leg 5L is less clear. It could be due to descent of streamlines that brings air with lower B down to the level of leg 5L in the lee. Alternatively, it could be due in part to drift in p_m associated with synoptic variations that are not fully removed by our p'_{synop} correction (see Fig. A1).

The wake is also distinct in its thermodynamic properties. It is potentially warmer by about 1–1.5 K and

drier by about $0.5\text{--}2\text{ g kg}^{-1}$. Three plausible contributions to the observed warming and drying are described below:

- 1) Downward transport of potentially warm and dry air in the plunging downslope flow (Fig. 11) could explain the wake’s character. This transport could be by turbulent vertical mixing in the plunging flow or by mean descent (facilitated by the upwind blocking discussed in section 4). Analysis of the upwind sounding (Fig. 2) indicates that mixing of air from the inversion base with low-level air could account for as much as $\Delta q_v \sim 0.5\text{ g kg}^{-1}$ and $\Delta T \sim 5\text{ K}$, explaining much of the observed wake signature. However, the actual degree of vertical transport cannot be ascertained from our observations.
- 2) Sensible heat fluxes imparted to the flow by the solar-heated surface of the island could contribute to the heating. We roughly estimate the sensible heat flux S by using temperature and downwelling-radiation data from Dominica’s Divide Ridge weather station (Fig. 1a) during RF13. We assume a surface albedo of 0.15, a surface emissivity of 0.97, and a Bowen ratio of 0.3 (we choose a high value for a tropical rain forest here to provide an upper bound) to estimate $S = 40\text{ W m}^{-2}$. We then estimate the net warming as

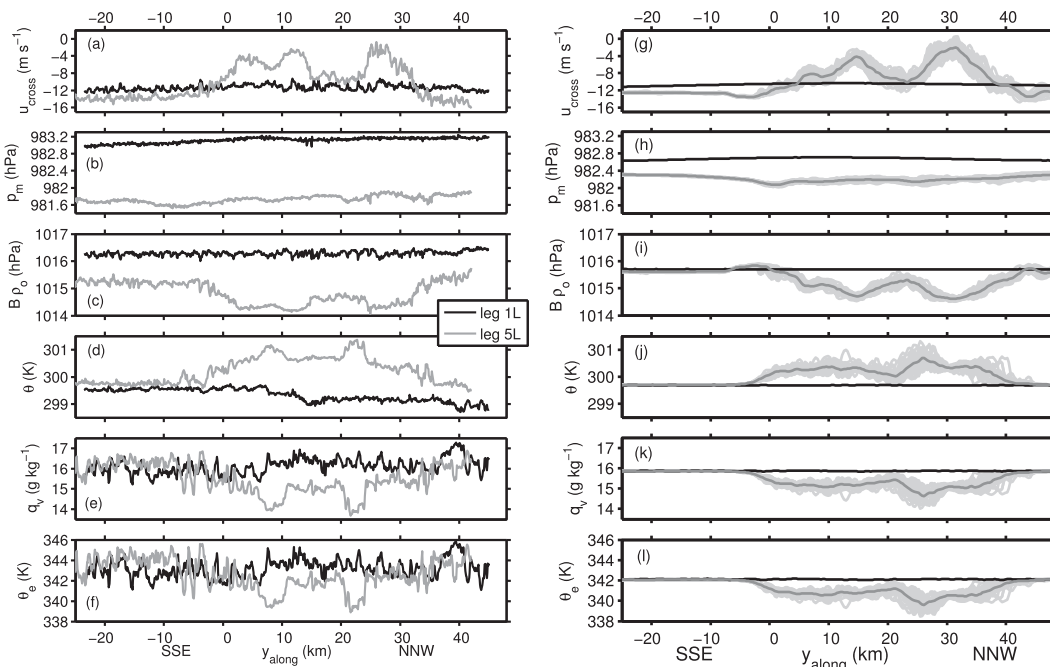


FIG. 13. Select dynamical variables along legs 1L and 5L (300 m MSL). (a)–(f) Observed $u_{\text{cross}}, p_m, B\rho_o, \theta, q_v, \theta_e$. (g)–(l) As in (a)–(f), respectively, but from the intermediate WRF domain ($\Delta x = 300\text{ m}$). In (g)–(l) light gray lines show instantaneous leg 5L values every 5 min over 2 h, whereas dark gray lines show the time mean.

$$\Delta T = \frac{L_{\text{cross}} S}{u_{\text{cross}} d c_p \rho}, \quad (2)$$

where d is the island-induced thermal boundary layer depth (assumed to be 500 m), L_{cross} is the island width (~ 20 km), $u_{\text{cross}} \sim 10 \text{ m s}^{-1}$, ρ is air density ($\sim 1 \text{ kg m}^{-3}$), and $c_p = 1004 \text{ J g kg}^{-1} \text{ K}^{-1}$. This predicts $\Delta T \sim 0.16 \text{ K}$ —a modest contribution.

- 3) In-cloud condensation and latent heating followed by precipitation could both warm and dry the low-level flow. Assuming that the low-level flow is dried similarly to the vertically integrated profile, we expect a low-level drying of about $\Delta q_v \sim q_{v,o} \text{DR} = 0.1 \text{ g kg}^{-1}$, where $q_{v,o}$ is the specific humidity of the upwind low-level air ($\sim 16 \text{ g kg}^{-1}$) and DR is the bulk drying ratio from Table 2 (0.007). This Δq_v is an order of magnitude less than observed drying, although it could be locally higher downwind of regions of heavy rainfall. We can estimate the associated warming as

$$\Delta T = \frac{L_v \Delta q_v}{c_p}. \quad (3)$$

This predicts a $\Delta T \sim 0.3 \text{ K}$ —a potentially important contribution.

To help distinguish between these mechanisms, we plot θ_e in Fig. 13f, which is conserved along streamlines even in the presence of latent heating and precipitation. Within the wake θ_e is either decreased (in the core) or unchanged (on the sides) relative to upwind. Thus, in the wake's core the drying is in excess of what can be explained by rainfall, pointing to an important role for vertical moisture transport.

b. Modeling

Output from the WRF simulation (Figs. 13g–l) reproduces most of the basic observed characteristics of the wake; it is decelerated, warmed, dried, and deficient in B relative to the upwind and surrounding air. The magnitude and structure of the low-level winds are particularly well reproduced, including the subwake structure and accelerated leeside air outside of the wake. The drop in p_m in the lee is less than the observed, which gives a reduced drop in B relative to observations. As a result, simulated acceleration of leeside air outside the wake is well described by conservation of B on level streamlines, whereas within the wake, turbulent processes appear to have reduced B and slowed the air. The magnitude of the warming and drying of the wake are generally well simulated. Since the simulation does not include any island surface heat fluxes, such fluxes do not appear to be responsible for the wake's thermodynamic character.

As in observations, θ_e is reduced in the wake, so condensation and precipitation alone cannot account for the wake's thermodynamic properties, and vertical transport is likely important. The wake shows significant turbulent fluctuations in time of u_{cross} , θ , and q_v .

The vertical structure of the wake air is compared with the upwind air in Fig. 14. Here the wake is identified as regions $-30 < x_{\text{cross}} < -8 \text{ km}$ with $|u_{\text{cross}}| < 7 \text{ m s}^{-1}$ at the fifth vertical model level ($\sim 280 \text{ m MSL}$). The spatial mean is shown with a gray line and spatial variability is shown with gray shading (see caption). Below 1 km MSL, the trade wind flow is strongly decelerated throughout the wake and stagnated or reversed at some locations. The low-level wake air is also deficient in B relative to the upwind (Fig. 14e). In fact, much of the wake has lower values of B than found at any height upwind. Thus, only dissipation—not simple vertical transport—can explain the low B (and hence weak winds) found in the wake.

Below 2 km, the wake is potentially warmed ($\Delta\theta \sim 0.75 \text{ K}$) and below 1.5 km it is dried ($\Delta q_v \sim -0.5 \text{ g kg}^{-1}$). As found in Fig. 13, the wake air below about 1.25 km MSL has reduced θ_e , indicating that the dryness of this air cannot be explained by precipitation alone. Aloft, around 2–2.75 km, the wake air is moister (as much as 0.9 g kg^{-1}) and has elevated θ_e . It appears that vertical mixing (by moist convection or the dry plunging flow) has homogenized these profiles in the vertical and reduced low-level moisture. Vertical gradients in θ are also reduced, which is consistent with vertical mixing. However, θ also shows a net warming throughout the profile that cannot be explained by mixing. This results from some combination of latent heating from rainfall and adiabatic warming from regional-scale descent (facilitated by upwind blocking). The resulting low-level dry air and reduced potential instability ($\Delta\theta_e/\Delta z$) may explain the frequently observed suppression of trade wind convection in the wakes of the Lesser Antilles and other islands.

7. Sensitivity experiments

To learn more about the physical mechanisms shaping mesoscale airflow, convection, and rainfall around Dominica two sensitivity experiments with WRF are conducted to isolate the dynamical roles of (i) latent heating and (ii) frictional drag over the terrain.

a. The role of latent heating and convection

As discussed above, latent heating from condensation followed by precipitation may have important impacts on the flow over Dominica by reducing blocking and warming the wake. Here, we isolate the role of latent

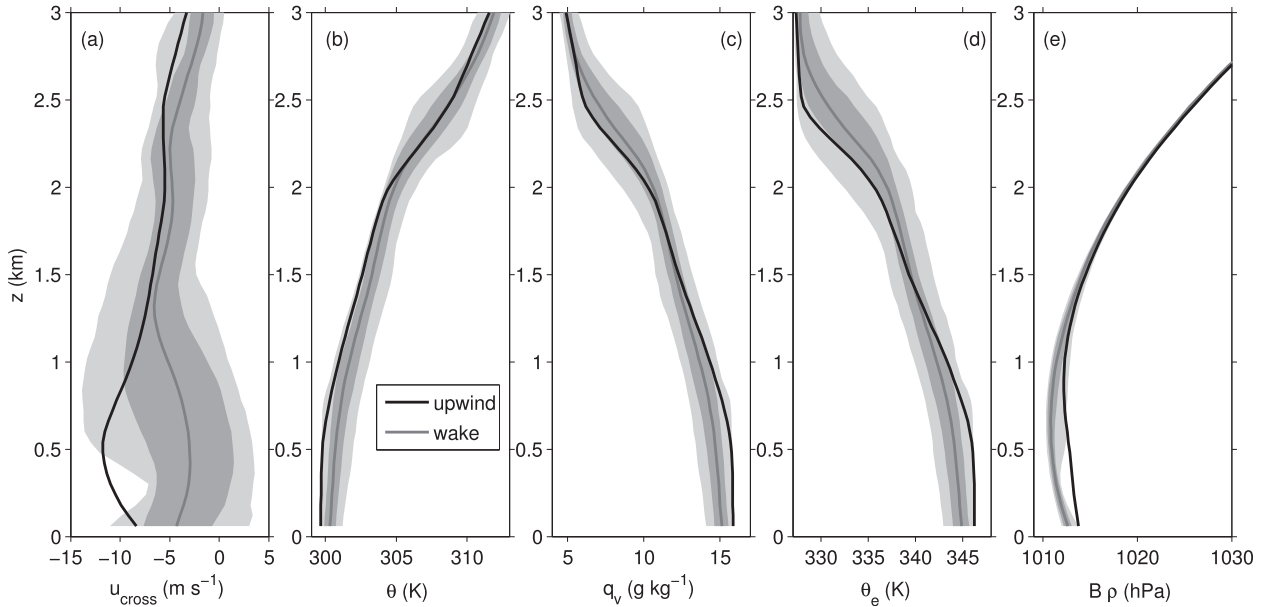


FIG. 14. Comparison of vertical profiles in the wake and upwind at model hour 7.75. Black lines show upwind profiles. Gray solid lines show horizontally averaged profiles from within the wake region (as defined in text). Shading corresponds to the 10th–90th (dark) and 1st–99th (light) percentiles of the spatial variability within the wake.

heating by conducting a simulation that is identical to the control, but latent heating (and cooling) due to microphysical phase changes is suppressed. This simulation is referred to as “noLH.” By suppressing latent heating, the dynamical regime is substantially altered. The resulting flow is no longer conditionally unstable and convective clouds are replaced by stratiform clouds.

The average rainfall rate from the noLH simulation is plotted in Fig. 15a. Even without latent heating and convection, heavy rain falls over the island. The mean rainfall over the high terrain is increased relative to the

control simulation owing to increases in both rainfall intensity and frequency. Rainfall also extends farther upwind than in the control case. In the absence of latent heating and convection, the DR increases to 1.4%. This suggests that while convection is effective at producing very high localized rainfall rates, its episodic nature may actually decrease the DR (e.g., Kirshbaum and Smith 2008; Cannon et al. 2012).

Low-level ($z = 300$ m) winds (Fig. 16a) reveal that without latent heating, flow deceleration and deflection upwind of the terrain are greatly improved, as

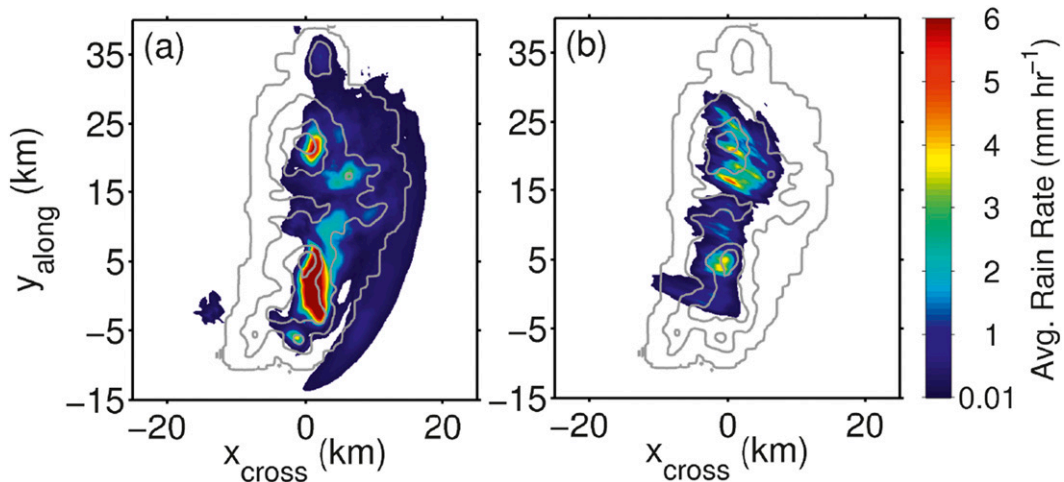


FIG. 15. Average precipitation rate, as in Fig. 4d, from sensitivity experiments (a) noLH and (b) watermtn.

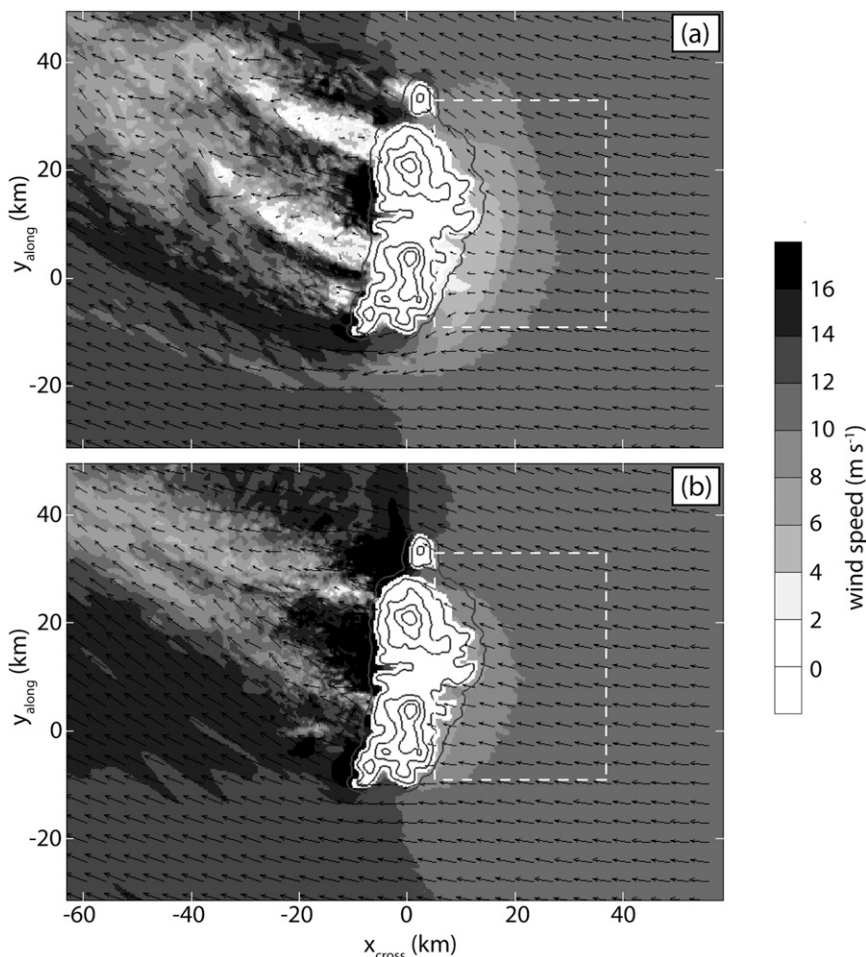


FIG. 16. Horizontal wind speed and vectors, as in Fig. 7, for sensitivity experiments (a) noLH and (b) watermtn.

found in previous studies (e.g., Jiang 2003). On the south-southeastern coast, the flow reaches stagnation and splits at low levels as found in observations and modeling of terrain-blocked flow (e.g., Rasmussen et al. 1989; Jiang 2003; Galewsky 2008). Comparing pressure along leg 2L (Fig. 17a) reveals that the noLH case has a larger positive p perturbation than the control. This occurs since latent heating in the control case acts to reduce upwind gravity wave ascent (Smith and Lin 1982). As a result of the larger p anomaly, the noLH case has much larger deceleration and lateral deflection along leg 2L (Figs. 17b–c). This increases the BR to 23%. Ascent of the trade winds over the blocked flow results in the upwind rainfall zone found in Fig. 15a.

A strong wake is still found in the noLH case (Fig. 18). It remains wider downwind of the terrain than in the control, and has more-distinct regions of deceleration downwind of the island's peaks. Figures 18a–c show that the dynamic structure of the wake, in terms of u_{cross} , p ,

and B , is barely affected by latent heating or the presence of convection. Furthermore, the potential warming of the wake is still strong at low levels (Fig. 18d) and aloft (not shown), suggesting that descent—not latent heating—is the primary source of the wake's warmth. The drying of the low-level wake is increased (Fig. 18e) owing to a combination of increased rainfall and increased downward transport of dry air (aided by the increased BR). Aloft, the moistening found in the control run (i.e., Fig. 14c) is eliminated (not shown), owing to either the stronger plunging flow or the lack of detrainment by convective clouds in the noLH run.

b. The role of island frictional drag

Surface drag over Dominica affects airflow dynamics by decelerating the low-level flow and helping to mix air vertically. Here, we isolate the role of enhanced island frictional drag by conducting a simulation that is identical to the control, but the roughness length for

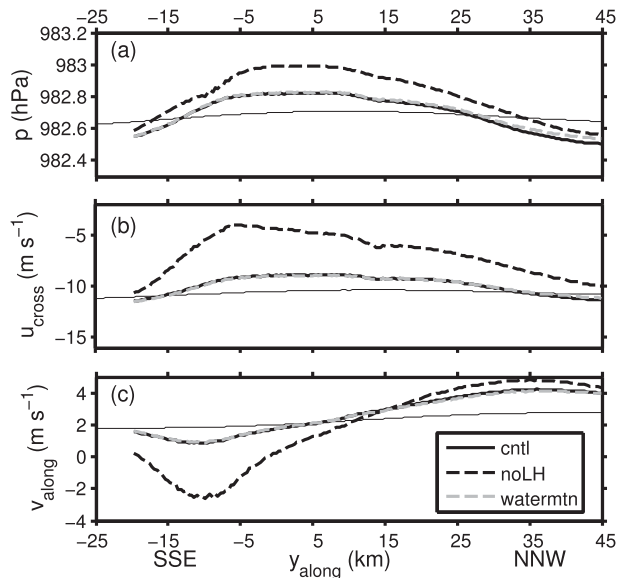


FIG. 17. Comparison of leg 2L variables for WRF sensitivity experiments. Thin black line shows time-mean values from leg 1L in the control simulation. Thick lines show leg 2L time-mean values for the control (cntl) and sensitivity experiments (noLH, watermtn) as indicated by key.

the surface layer scheme is computed in the same manner as over the ocean instead of using the much higher prescribed overisland value from the control (0.8 m).

The rainfall in this “watermtn” case is slightly less intense than in the control (Fig. 15b), with DR = 0.58%. This is likely due to reduced frictional convergence of the horizontal winds over the smoother island. The upwind flow and pressure fields show almost no response to the change in island roughness (Figs. 16b and 17), and BR is only reduced slightly to 15%.

Downwind of the terrain, flow deceleration in the wake is reduced. Additionally, the jets of wind downwind of the saddle and the island’s flanks extend several kilometers farther (Fig. 16b). Figures 18a–c show that without the rough terrain, the deceleration of u_{cross} is reduced, resulting in a smaller drop in B . Still, both variables show distinct wake signatures, suggesting that both frictional dissipation at the surface and the turbulent plunging flow play important roles in generating the observed wake. The warming and drying of the wake are not changed substantially (Figs. 18d–f), indicating that mixing from turbulence generated at the surface is not responsible for the thermodynamic structure of the wake.

8. Summary and conclusions

Over the mountainous Caribbean island of Dominica, strong, moist, conditionally unstable trade winds are

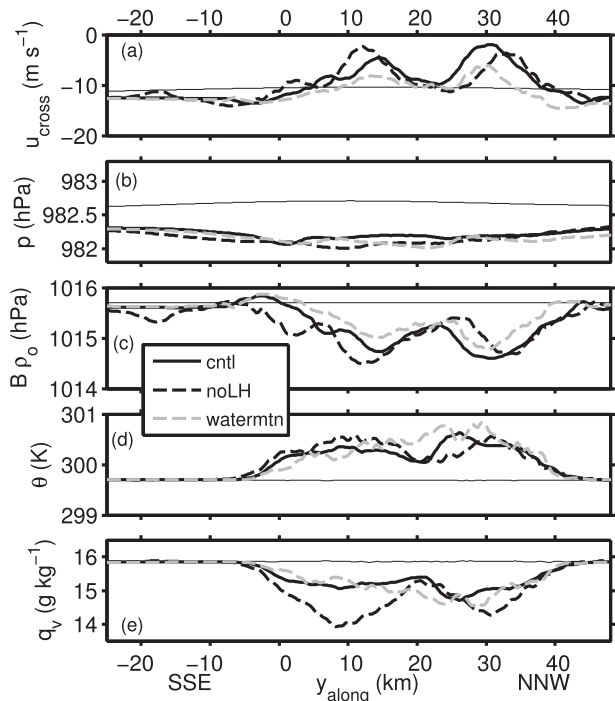


FIG. 18. Comparison of leg 5L variables for WRF sensitivity experiments. Thin black line shows time-mean values from leg 1L in the control simulation. Thick lines show leg 5L time-mean values for the control (cntl) and sensitivity experiments (noLH, watermtn) as indicated by key.

lifted by the terrain, initiating vigorous shallow cumulus convection and rainfall. Airborne observations and quasi-idealized cloud-resolving simulations were used to describe the mesoscale dynamics of this flow and to investigate the governing processes. Simulations reproduced all the prominent dynamical features despite mixed results in reproducing the observed rainfall.

Mesoscale airflow over Dominica controls the life cycle of convection over the island. Upwind of the terrain, little orographic flow deflection or lifting occurs. As a result, there is little upwind enhancement of convection or rainfall. The lack of upwind deformation is due in part to latent heating in convection over the terrain. Over the windward slopes, orographic lifting is very effective at initiating vigorous cumulus convection. Although convective cells bring heavy showers, they do not appear to enhance the time-mean rainfall.

As air flows over the island’s crest, it quickly transitions to a plunging, dry, and turbulent downslope wind. A low-level downslope jet is capped by a pocket of near-stagnant air above, and turbulence is likely generated atop the jet by shear instabilities. The downslope wind configuration is similar to those found in observations and modeling of dry stratified flows, despite the conditionally unstable atmosphere and vigorous moist

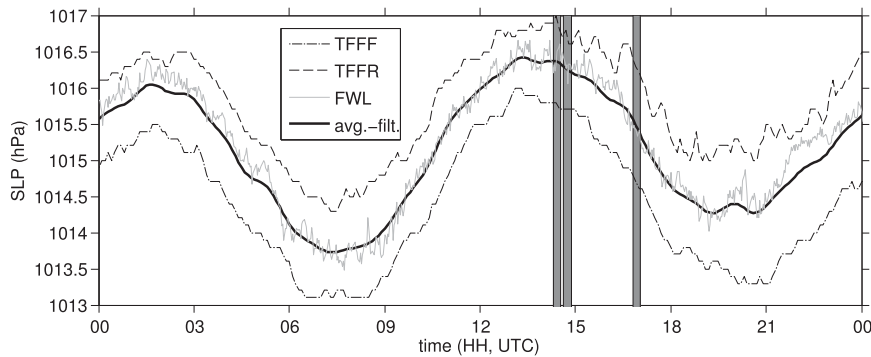


FIG. A1. Regional-scale pressure variations. The three thin lines show time series of SLP from surface stations on Martinique (TFFF), Guadeloupe (TFFR), and Dominica (FWL) on 27 Apr 2011 (see Fig. 1a for locations). Vertical bars correspond to the times of legs 1L, 2L, and 5L during RF13. The thick line shows the average of these three time series after a low-pass filter has been applied. The filtered data are used to remove regional-scale pressure variations from the aircraft-measured pressures.

convection just upwind. This plunging flow eliminates convective clouds but allows for some spillover of orographic rain to the lee coast.

In the lee of the terrain there is a distinct wake of transformed air. This air is decelerated throughout the trade wind layer because of turbulent dissipation associated with shear instabilities atop the plunging flow and frictional drag over the island's rough surface. In the lowest kilometer, the air is also warmed and dried. The warming and drying is caused primarily by vertical transport in the turbulent plunging flow, with latent heating and rainfall playing a secondary role. The low-level drying of the wake effectively suppresses convection and rainfall downwind of the terrain. The rain shadow in the lee of Dominica is not caused by water depletion from rainfall, since the drying ratio of the flow is very modest.

Since mesoscale airflow controls the convection and rainfall over Dominica, it seems likely that sensitivity of mesoscale circulations to incoming flow characteristics determine variability in the form and intensity of convection and rainfall. For instance, at low wind speeds, circulations over Dominica appear to be thermally driven by solar heating (Smith et al. 2012). We are currently examining other research flights and long-term datasets to improve understanding of large-scale controls on tropical orographic convection and rainfall, as well as downslope winds and downstream wakes. These efforts will be useful for the development of parameterizations in models that cannot resolve convection and for forecasting metrics.

Acknowledgments. This work benefited from conversations with Dan Kirshbaum. The manuscript was improved thanks to comments of Bart Geerts and two

anonymous reviewers. Tom Parish processed the differentially corrected GPS data. Robert Warren corrected the airborne temperature data for probe-wetting biases. Sam Haimov, Jeff French, Larry Oolman, and the UWKA team provided invaluable support and advice in the field. Philippe Palany and Meteo France provided data from operational radars and surface stations. WRF simulations were conducted using facilities of the Yale University Faculty of Arts and Sciences High Performance Computing Center. This work was supported by NSF Grant ATM-0930356. JRM's participation was also supported by the Yale Geology and Geophysics Flint Postdoctoral Fellowship.

APPENDIX

Calculation of Mesoscale Pressure Anomalies

Before airborne pressure measurements can be used to investigate mesoscale dynamics, the static pressure measured by the aircraft must be corrected to remove signals that mask the terrain-induced pressure anomalies.

First, the variations in aircraft altitude along a nominally level leg (about ± 10 m) are large enough to have significant effects on the measured pressure (about ± 1 hPa). We remove these altitude-related pressure anomalies by using the aircraft altitude to calculate the pressure anomaly caused by displacement from the desired flight level in a hydrostatically balanced atmosphere as $\bar{\rho}g(z - z_{\text{leg}})$, where $\bar{\rho}$ is the mean air density along the leg and $z_{\text{leg}} = 300$ m for the low-level legs. To compute this correction adequately requires very accurate and precise measurements of aircraft altitude. Only through the use of GPS-based altitudes that were differentially corrected using a base station deployed on

Martinique [following Parish et al. (2007)] were we able to achieve satisfactory results.

Second, a semidiurnal cycle in pressure is a prominent feature of the tropical atmosphere due to global atmospheric tides. This oscillation can be seen in sea level pressure (SLP) measurements made by surface stations on Dominica, Martinique, and Guadeloupe (Fig. A1). The global scale associated with these oscillations mean that they have minimal dynamical significance for the mesoscale flow over Dominica [$\Delta P/\Delta x \sim (2 \text{ hPa})/(10^4 \text{ km}) = 2 \times 10^{-4} \text{ hPa km}^{-1}$]. However, they produce significant pressure changes over the course of a research flight that may obscure mesoscale pressure differences between flight legs (Fig. A1). We wish to remove this signal, and any other synoptic-scale or diurnally forced pressure anomalies, from our aircraft data. To do so, we average 6-min SLP data from the three stations mentioned above, apply a low-pass ninth-order Butterworth filter with a 24-cpd frequency cutoff (see Fig. A1), and subtract out the mean from the period of the research flight. This “synoptic-scale” pressure anomaly p'_{synop} is then subtracted from the aircraft-measured pressure.

The final “mesoscale pressure” then takes the form

$$p_m = p - \bar{\rho}g(z - z_{\text{leg}}) - p'_{\text{synop}}, \quad (\text{A1})$$

with symbols defined as above.

REFERENCES

- Banta, R., 1990: The role of mountain flows in making clouds. *Atmospheric Processes over Complex Terrain, Meteor. Monogr.*, No. 45, Amer. Meteor. Soc., 229–283.
- Biasutti, M., S. E. Yuter, C. D. Burleyson, and A. H. Sobel, 2012: Very high resolution rainfall patterns measured by TRMM precipitation radar: Seasonal and diurnal cycles. *Climate Dyn.*, **39** (1–2), 239–258, doi:10.1007/s00382-011-1146-6.
- Bryan, G. H., J. C. Wyngaard, and J. M. Fritsch, 2003: Resolution requirements for the simulation of deep moist convection. *Mon. Wea. Rev.*, **131**, 2394–2416.
- Cannon, D. J., D. J. Kirshbaum, and S. L. Gray, 2012: Under what conditions does embedded convection enhance orographic precipitation? *Quart. J. Roy. Meteor. Soc.*, **138**, 391–406, doi:10.1002/qj.926.
- Carbone, R. E., W. A. Cooper, and W. C. Lee, 1995: Forcing of flow reversal along the windward slopes of Hawaii. *Mon. Wea. Rev.*, **123**, 3466–3480.
- , J. D. Tuttle, W. A. Cooper, V. Grubisic, and W. C. Lee, 1998: Trade wind rainfall near the windward coast of Hawaii. *Mon. Wea. Rev.*, **126**, 2847–2863.
- Chen, Y. L., and A. J. Nash, 1994: Diurnal variation of surface airflow and rainfall frequencies on the island of Hawaii. *Mon. Wea. Rev.*, **122**, 34–56.
- Clark, T. L., and W. R. Peltier, 1984: Critical-level reflection and the resonant growth of nonlinear mountain waves. *J. Atmos. Sci.*, **41**, 3122–3134.
- Cohard, J. M., and J. P. Pinty, 2000: A comprehensive two-moment warm microphysical bulk scheme. I: Description and tests. *Quart. J. Roy. Meteor. Soc.*, **126**, 1815–1842, doi:10.1002/qj.49712656613.
- , —, and C. Bedos, 1998: Extending Twomey’s analytical estimate of nucleated cloud droplet concentrations from CCN spectra. *J. Atmos. Sci.*, **55**, 3348–3357.
- Durran, D. R., 1986: Another look at downslope windstorms. 1. The development of analogs to supercritical-flow in an infinitely deep, continuously stratified fluid. *J. Atmos. Sci.*, **43**, 2527–2543.
- , and J. B. Klemp, 1983: A compressible model for the simulation of moist mountain waves. *Mon. Wea. Rev.*, **111**, 2341–2361.
- Epifanio, C. C., and T. T. Qian, 2008: Wave–turbulence interactions in a breaking mountain wave. *J. Atmos. Sci.*, **65**, 3139–3158.
- Gabersek, S., and D. R. Durran, 2004: Gap flows through idealized topography. Part I: Forcing by large-scale winds in the non-rotating limit. *J. Atmos. Sci.*, **61**, 2846–2862.
- Galewsky, J., 2008: Orographic clouds in terrain-blocked flows: An idealized modeling study. *J. Atmos. Sci.*, **65**, 3460–3478.
- Holland, J. Z., and W. Rasmusson, 1973: Measurements of atmospheric mass, energy, and momentum budgets over a 500-kilometer square of tropical ocean. *Mon. Wea. Rev.*, **101**, 44–55.
- Houze, R. A., 2012: Orographic effects on precipitating clouds. *Rev. Geophys.*, **50**, RG1001, doi:10.1029/2011RG000365.
- Janjic, Z., 1996: The surface layer in the NCEP Eta Model. *Proc. 11th Conf. on Numerical Weather Prediction*, Norfolk, VA, Amer. Meteor. Soc., 354–355.
- Jiang, Q. F., 2003: Moist dynamics and orographic precipitation. *Tellus*, **55A**, 301–316.
- , and R. B. Smith, 2003: Cloud timescales and orographic precipitation. *J. Atmos. Sci.*, **60**, 1543–1559.
- Kirshbaum, D. J., and R. Smith, 2008: Temperature and moist-stability effects on midlatitude orographic precipitation. *Quart. J. Roy. Meteor. Soc.*, **134**, 1183–1199, doi:10.1002/qj.274.
- , and R. B. Smith, 2009: Orographic precipitation in the tropics: Large-eddy simulations and theory. *J. Atmos. Sci.*, **66**, 2559–2578.
- , and A. L. M. Grant, 2012: Invigoration of cumulus cloud fields by mesoscale ascent. *Quart. J. Roy. Meteor. Soc.*, **138**, 2136–2150, doi:10.1002/qj.1954.
- Klemp, J., J. Dudhia, and A. Hassiotis, 2008: An upper gravity-wave absorbing layer for NWP applications. *Mon. Wea. Rev.*, **136**, 3987–4004.
- Knievel, J. C., G. H. Bryan, and J. P. Hacker, 2007: Explicit numerical diffusion in the WRF model. *Mon. Wea. Rev.*, **135**, 3808–3824.
- Lilly, D. K., 1978: Severe downslope windstorm and aircraft turbulence event induced by a mountain wave. *J. Atmos. Sci.*, **35**, 59–77.
- Milbrandt, J., and M. Yau, 2005: A multimoment bulk microphysics parameterization. Part II: A proposed three-moment closure and scheme description. *J. Atmos. Sci.*, **62**, 3065–3081.
- Nesbitt, S. W., and A. M. Anders, 2009: Very high resolution precipitation climatologies from the Tropical Rainfall Measuring Mission precipitation radar. *Geophys. Res. Lett.*, **36**, L15815, doi:10.1029/2009GL038026.
- Pan, F. F., and R. B. Smith, 1999: Gap winds and wakes: SAR observations and numerical simulations. *J. Atmos. Sci.*, **56**, 905–923.

- Parish, T. R., M. D. Burkhardt, and A. R. Rodi, 2007: Determination of the horizontal pressure gradient force using global positioning system on board an instrumented aircraft. *J. Atmos. Oceanic Technol.*, **24**, 521–528.
- Rasmussen, R. M., P. Smolarkiewicz, and J. Warner, 1989: On the dynamics of Hawaiian cloud bands: Comparison of model results with observations and island climatology. *J. Atmos. Sci.*, **46**, 1589–1608.
- Rauber, R. M., and Coauthors, 2007: Rain in shallow cumulus over the ocean: The RICO campaign. *Bull. Amer. Meteor. Soc.*, **88**, 1912–1928.
- Reisner, J. M., and P. K. Smolarkiewicz, 1994: Thermally forced low Froude number flow past three-dimensional obstacles. *J. Atmos. Sci.*, **51**, 117–133.
- Roe, G. H., 2005: Orographic precipitation. *Annu. Rev. Earth Planet. Sci.*, **33**, 645–671.
- Rotunno, R., and R. Houze, 2007: Lessons on orographic precipitation from the Mesoscale Alpine Programme. *Quart. J. Roy. Meteor. Soc.*, **133**, 811–830.
- Schar, C., and R. B. Smith, 1993: Shallow-water flow past isolated topography. 1. Vorticity production and wake formation. *J. Atmos. Sci.*, **50**, 1373–1400.
- Sheridan, P. F., and S. B. Vosper, 2005: Numerical simulations of rotors, hydraulic jumps and eddy shedding in the Falkland Islands. *Atmos. Sci. Lett.*, **6** (4), 211–218, doi:10.1002/asl.118.
- Skamarock, W., and M. Weisman, 2009: The impact of positive-definite moisture transport on NWP precipitation forecasts. *Mon. Wea. Rev.*, **137**, 488–494.
- , and Coauthors, 2008: A description of the Advanced Research WRF version 3. NCAR Tech. Note NCAR/TN-475+STR, 113 pp. [Available online at http://www.mmm.ucar.edu/wrf/users/docs/arw_v3_bw.pdf.]
- Smith, C. M., and E. D. Skillingstad, 2011: Effects of inversion height and surface heat flux on downslope windstorms. *Mon. Wea. Rev.*, **139**, 3750–3764.
- Smith, R. B., 1985: On severe downslope winds. *J. Atmos. Sci.*, **42**, 2597–2603.
- , 1987: Aerial observations of the Yugoslavian Bora. *J. Atmos. Sci.*, **44**, 269–297.
- , 1989: Mountain-induced stagnation points in hydrostatic flow. *Tellus*, **41A**, 270–274, doi:10.1111/j.1600-0870.1989.tb00381.x.
- , 2006: Progress on the theory of orographic precipitation. *Tectonics, Climate, and Landscape Evolution*, S. Willett et al., Eds., Geological Society of America Special Papers, Vol. 398, 434 pp.
- , and Y. L. Lin, 1982: The addition of heat to a stratified airstream with application to the dynamics of orographic rain. *Quart. J. Roy. Meteor. Soc.*, **108**, 353–378.
- , A. C. Gleason, P. A. Gluhosky, and V. Grubisic, 1997: The wake of St. Vincent. *J. Atmos. Sci.*, **54**, 606–623.
- , P. Schafer, D. J. Kirshbaum, and E. Regina, 2009: Orographic precipitation in the tropics: Experiments in Dominica. *J. Atmos. Sci.*, **66**, 1698–1716.
- , and Coauthors, 2012: Orographic precipitation in the tropics: The Dominica experiment. *Bull. Amer. Meteor. Soc.*, **93**, 1567–1579.
- Tabary, P., 2007: The new French operational radar rainfall product. Part I: Methodology. *Wea. Forecasting*, **22**, 393–408.
- , J. Desplats, K. D. Khac, F. Eideliman, C. Gueguen, and J. C. Heinrich, 2007: The new French operational radar rainfall product. Part II: Validation. *Wea. Forecasting*, **22**, 409–427.
- Wang, Y. G., and B. Geerts, 2009: Estimating the evaporative cooling bias of an airborne reverse flow thermometer. *J. Atmos. Oceanic Technol.*, **26**, 3–21.